The Lunar Geophysical Network Landing Sites Science Rationale

Haviland Heidi Fuqua, Renee C. Weber, Clive R. Neal, Philippe Lognonné, Raphaël F. Garcia, Nicholas Schmerr, Seiichi Nagihara, Robert Grimm, Douglas G. Currie, Simone Dell'Agnello, et al.

The Planetary Science Journal, 3:40 (21pp), 2022 February https://doi.org/10.3847/PSJ/ac0f82

The Lunar Geophysical Network Landing Sites Science Rationale

Heidi Fuqua Haviland[1], Renee C. Weber[2], Clive R. Neal[3], Philippe Lognonné[3], Raphaël F. Garcia[4], Nicholas Schmerr[5], Seiichi Nagihara[6], Robert Grimm[7], Douglas G. Currie[8], Simone Dell'Agnello[9], Thomas R. Watters[10], Mark P. Panning[11], Catherine L. Johnson[12,13], Ryuhei Yamada[14], Martin Knapmeyer[15], Lillian R. Ostrach[16], Taichi Kawamura[3], Noah Petro[17], and Paul M. Bremner[1]
[1] NASA Marshall Space Flight Center, Science and Technology Office, 320 Sparkman Avenue, NSSTC, Huntsville, AL 35820, USA; heidi.haviland@nasa.gov
[2] University of Notre Dame, Dept. Civil & Env. Eng. & Earth Sciences, Notre Dame, IN 46556, USA
[3] Planetology And Space Sciences - IPGP, Paris Rive Gauche - LAMARCK, Université de Paris, 35 rue Hélène Brion, 75013, Paris, France
[4] Department of Geology, University of Maryland, 8000 Regents Drive, College Park, MD 20742, USA
[5] Department of Geosciences, Texas Tech University, Lubbock, TX 79409, USA
[6] Southwest Research Institute, 1050 Walnut Street, Suite 300, Boulder, CO 80302, USA
[7] Department of Physics, University of Maryland, College Park, MD 20904, USA
[8] Istituto Nazionale di Fisica Nucleare, Laboratori Nazionali di Frascati (INFN-LNF), I-00044, Frascati, (Rome), Italy
[9] Center for Earth and Planetary Studies, National Air and Space Museum, Smithsonian Institution, P.O. Box 37012, Washington, DC 20560, USA
[10] NASA Jet Propulsion Lab, 4800 Oak Grove Drive, Pasadena, CA 91109, USA
[11] Department of Earth, Ocean and Atmospheric Sciences, University of British Columbia, Vancouver, BC, V6T 1Z4, Canada
[12] Planetary Science Institute, 1700 E Fort Lowell, Suite 106, Tucson AZ 85719, USA
[13] University of Aizu, Aizu-Wakamatsu, Fukushima Pref. 965-8580, Japan
[14] Deutsches Zentrum für Luft- und Raumfahrt, Institut für Planetenforschung, Rutherfordstr. 2, 12489 Berlin, Germany
[15] U.S. Geological Survey, Astrogeology Science Center, 2255 N Gemini Drive, Flagstaff, AZ 86001, USA
[16] NASA Goddard Space Flight Center, Mail Code 698, Greenbelt, MD 20771, USA
[17] ISAE-SUPAERO, 10 ave E. Belin, F-31400 Toulouse, France
Received 2020 November 16; revised 2021 May 11; accepted 2021 June 11; published 2022 February 18

Abstract

The Lunar Geophysical Network (LGN) mission is proposed to land on the Moon in 2030 and deploy packages at four locations to enable geophysical measurements for 6–10 yr. Returning to the lunar surface with a long-lived geophysical network is a key next step to advance lunar and planetary science. LGN will greatly expand our primarily Apollo-based knowledge of the deep lunar interior by identifying and characterizing mantle melt layers, as well as core size and state. To meet the mission objectives, the instrument suite provides complementary seismic, geodetic, heat flow, and electromagnetic observations. We discuss the network landing site requirements and provide example sites that meet these requirements. Landing site selection will continue to be optimized throughout the formulation of this mission. Possible sites include the P-5 region within the Procellarum KREEP Terrane (PKT; (lat: 15°; long: −35°), Schickard Basin (lat: −44.°3; long: −55.°1), Crisium Basin (lat: 18.°5; long: 61.°8), and the farside Korolev Basin (lat: −2.°4; long: −159.°3). Network optimization considers the best locations to observe seismic core phases, e.g., ScS and PKP. Ray path density and proximity to young fault scarps are also analyzed to provide increased opportunities for seismic observations. Geodetic constraints require the network to have at least three nearside stations at maximum limb distances. Heat flow and electromagnetic measurements should be obtained away from terrane boundaries and from magnetic anomalies at locations representative of global trends. An in-depth case study is provided for Crisium. In addition, we discuss the consequences for scientific return of less than optimal locations or number of stations.

Unified Astronomy Thesaurus concepts: Lunar interior (959); Lunar seismology (973); Lunar composition (948); Lunar rilles (971); Lunar science (972); The Moon (1692)

1. Introduction

Understanding the interior properties of the Moon, including the size and state of the core, is of utmost importance to the future of lunar and planetary science. While a wealth of information has been gleaned from Apollo-era investigations and subsequent orbiters, gaps remain in our current understanding (Neal et al. 2020). A long-lived next-generation network of surface geophysical stations, the Lunar Geophysical Network (LGN), will provide simultaneous multipoint geophysical observations across four complementary disciplines: seismology, geodesy, heat flow, and electromagnetics from around the Moon. Together these observations will unlock key outstanding issues regarding the lunar interior, including the existence of, size of, and state of the inner core; the presence of a deep mantle partial melt layer; mantle thermal state; and composition, including lateral and vertical heterogeneity.

The purpose of this paper is to discuss the science driving the LGN mission landing sites. In particular, we discuss a network composed of four sites with seismic, laser ranging (on the nearside), heat flow, and magnetotelluric (MT) measurements made at each. We provide an in-depth discussion of a possible site in Mare Crisium, as a case study for future mission planning methodology for locating where within a landing site is best for the LGN mission as a whole. We begin with example landing sites and note that these will continue to evolve through the formulation of the mission. We also note that the LGN

mission requires continuous measurements to be made throughout multiple lunar day/night cycles.

In addition to LGN, there are several exciting upcoming opportunities for missions to the lunar surface, including short-duration (<14 Earth days, limited to operate within the daytime without night survival) Commercial Lunar Payload Services (CLPS) missions, the future NASA Artemis program providing a human presence at the lunar surface, and international missions such as the European Lunar Geophysical Observatory (ELGO; Garcia et al. 2020). In this paper, we focus on the four LGN stations as primary nodes to achieve the mission science objectives with a launch in 2030. Other opportunities may help improve instrument performance, improve risk mitigation, and provide additional nodes in support of the LGN network; however, discussion of these opportunities is beyond the scope of this paper. We first provide a description of the LGN mission, including science questions, objectives, and traceability; an overview of the communications architecture required by this mission; and required instrument performances (Section 2). We highlight four potential landing sites and review the implications of optimizing the locations of these primary network nodes, as well as the scientific consequences and priorities of needing to remove one or more landing sites. In addition, we detail the seismic, geodetic, heat flow, and electromagnetic (EM) science requirements for the network (Section 3). We then provide a detailed study on how to locate a surface site within Mare Crisium as a case study (Section 4). Lastly, we conclude by highlighting next steps for this mission in determining landing sites (Section 5). The reader is directed to Table A1 for a list of all acronyms used.

2. The LGN Mission Overview

The goal of the LGN mission is to understand the evolution of terrestrial planets, from their initial stages of formation, differentiation, and subsequent persistence (or lack) of internal dynamics into the present (Neal et al. 2020). Terrestrial planets all share a common structural framework (e.g., crust, mantle, core) that is developed very shortly after formation and that determines subsequent evolution (e.g., McCulloch 1987; Elkins-Tanton et al. 2003, 2011; Elkins-Tanton 2008; Brown & Elkins-Tanton 2009; Charlier et al. 2013; Maurice et al. 2017; Ikoma et al. 2018). The Moon is a natural target for this type of geophysical network mission, as it presents an opportunity to study an internal heat engine that waned early in planetary evolution and thereby enabled preservation of the initial magma ocean differentiation event (Smith et al. 1970; Wood et al. 1970). Such information has been lost on Earth, due to crustal recycling and weathering of our most ancient rocks, and also on Mars and Venus, due to their larger sizes and heat engines, producing prolonged volcanic activity and resurfacing that is thought to have continued to the present day (e.g., Hartmann 1999; Stofan et al. 2016; Filiberto et al. 2020). The lunar initial differentiation model is supported by analyses of returned Apollo basaltic samples, which are consistent with derivation from a source composed of cumulates that crystallized from an initial magma ocean and subsequently underwent an overturn event (Taylor & Jakes 1974; Snyder et al. 1992, 1997).

An LGN mission should (1) be "better than Apollo" (see Section 2.1 below), (2) permit a global distribution of stations, including the farside, and (3) allow for redundancy as part of the baseline mission. Each lander should contain a sensitive broadband seismometer, laser retroreflectors, heat flow probes, and EM sounders. The landers should be long-lived (>6 yr, with a goal of 10 yr) to maximize science and allow other nodes to be added by international and commercial partners during the lifetime of the mission, thus increasing the fidelity and value of the data obtained.

The baseline LGN mission architecture requires an orbiter to serve as the primary communication relay for the farside lander. This concept requires mission operations to manage command and control of the orbiter and four landers. The mission operations team should primarily utilize direct-to-Earth communication links to talk to all landers on the nearside of the Moon. Operations will have the option to communicate with the nearside landers via the orbiter relay communication links for redundancy.

2.1. Science Questions and Objectives

Our first look into the Moon's interior came from the Apollo Lunar Surface Experiment Packages (ALSEP) that deployed surface magnetometers, placed laser retroreflector arrays, installed seismometers that detected moonquakes and meteorite impacts, and took heat flow measurements—key geophysical information that has advanced our knowledge of the Moon's internal structure, evolution, and dynamics. However, it is now evident that, due in part to the relatively narrow geographical extent of the Apollo passive seismic network, our understanding of the lunar interior, and especially the deep interior and core, remains incomplete (Figure 1). For example, garnet has been hypothesized to exist below ~500 km within the Moon (e.g., Anderson 1975; Hood 1986; Hood & Jones 1987; Neal 2001). However, interpretations based on the limited seismic data are ambiguous. For example, Nakamura et al. (1974) and Nakamura (1983) suggested that higher velocities in the middle mantle (>500 km) could be indicative of an increased proportion of Mg-rich olivine. This has implications for the bulk composition of the Moon, especially for Al_2O_3. For example, GRAIL data have been used to constrain the crustal contribution to bulk Al_2O_3 of 1.7–2.1 wt.% (Wieczorek et al. 2013) and conclude that the bulk Al_2O_3 content of the Moon is lower than the 6.1 wt.% of the Taylor Bulk Moon composition (Taylor 1982). However, Wieczorek et al. (2013) note that Al_2O_3 in the mantle derived from Apollo seismic data has a broad range (2.0–6.7 wt.%) for the upper and lower mantle. Khan et al. (2006b) demonstrated that no mid-mantle velocity jump was required to fit the Apollo seismic data with a homogeneous mantle bulk composition. Stable phases have been calculated in compositional models for the lunar interior, along with their respective seismic properties. The results suggest that garnet would be a minor stable phase in the middle mantle of the Moon between 270 and 500 km but would be a significant phase in the lower lunar mantle between 500 and 1262 km (e.g., Khan et al. 2006b; Kuskov et al. 2014, 2019 and references therein). The existing seismic data are insufficient to be used to discriminate between these models and yield accurate estimates of lunar bulk composition.

Additionally, the identification of different lunar surface terranes from new global surface compositional data has produced a shift in our understanding of the global evolution model of the Moon (Jolliff et al. 2000; Laneuville et al. 2018). These data demonstrate that there is a fundamental limitation to the ALSEP geophysical data sets, as all were collected in or very near one anomalous region, the Procellarum KREEP

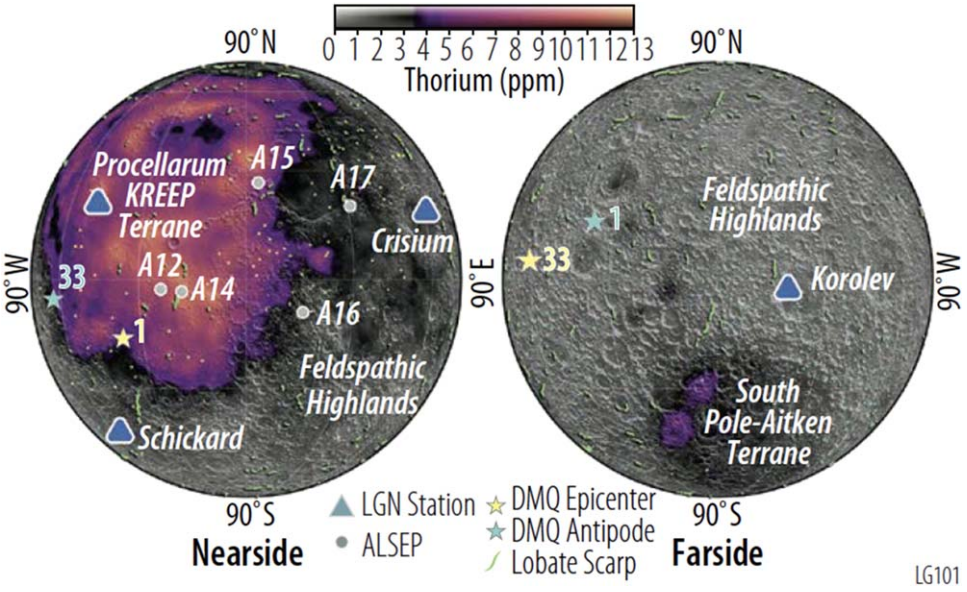

Figure 1. Example LGN station locations (blue triangles) compared to Apollo (gray circles). LGN stations will be placed across major lunar terranes and enable new interrogation of the deep lunar interior and tectonic evolution. The proposed LGN stations are positioned to take advantage of (1) possible recent lobate scarp seismicity (green lines; Watters et al. 2019) and (2) known DMQ clusters and their antipodes (yellow and cyan stars, respectively). The two most active nearside and farside DMQ clusters (A01 and A33) are highlighted. DMQ cluster epicenters, each exhibiting characteristically repeating waveforms between 550 and 1420 km in depth, are thought to be caused by the tidal forces of the Earth–Moon system at intervals of 27–29 days (Weber et al. 2009). Their antipodes, where core-transmitted phases would be focused, are located on the opposite side of the Moon (Nakamura 2005). The LGN network is designed to geophysically interrogate the internal structure, temperature, composition, and tectonics/seismicity both in the Feldspathic Highlands (unsampled by Apollo) and within the Procellarum KREEP terrane, outlined by the Lunar Prospector thorium abundance (Lawrence et al. 2000). Shaded surface relief is derived from LOLA topography (Smith et al. 2017).

(potassium, rare-earth elements, phosphorus) Terrane (PKT) (Figure 1). Subsequent orbital missions have expanded the global geophysical picture of the interior (e.g., Lunar Prospector (LP), Gravity Recovery And Interior Laboratory (GRAIL), Kaguya, Lunar Reconnaissance Orbiter (LRO), etc.), but only a landed long-lived geophysical network can address the significant questions that remain unanswered by Apollo:

1. How does the overall composition and structure of the Moon inform us about initial differentiation of terrestrial planets?
2. What is the state, structure, and composition of the mantle, and is it consistent with the lunar magma ocean hypothesis (or are there resolvable discontinuities)?
3. What range of bulk compositional models for the crust, mantle, and core are compatible with combined LGN and previous data sets?
4. What is the present heat budget, and how could the Moon experience magmatism for >3 billion years?
5. What is the crust and mantle heterogeneity within and between different terranes?
6. Based on a constrained size, state, and composition, how did the lunar core form, and could it have supported a global magnetosphere (as indicated by sample analyses—e.g., Hiesinger et al. 2003; Mighani et al. 2020)?

New geophysical data are needed to address these questions and add greater fidelity to data sets already obtained. The Apollo seismic network possessed a narrow aperture and was emplaced on the edge of and within a special crustal terrane, but it has necessarily been used to extrapolate global interior properties. For example, the GRAIL gravity data that inform crustal thickness are constrained by Apollo seismic data (Khan & Mosegaard 2002; Lognonne et al. 2003; Chenet et al. 2006), but the fidelity across the lunar surface is poor owing to the narrow aperture of the Apollo passive seismic network and localization in the thinned and likely anomalous nearside crust of the PKT (e.g., Hood 1986). Another example are the large discrepancies among the size and nature of the lunar core defined by seismic, lunar laser retroreflector (LLR), and GRAIL data, which reflect the lack of fidelity in Apollo seismic and ongoing LLR data (e.g., Williams et al. 2014). Therefore, the fundamental purpose of the LGN mission is to broadly distribute landers with seismometers, heat flow probes, Next Generation Lunar Retroreflectors (NGLR), and EM sounders around the Moon, including on the farside, that are placed well within the boundaries of varied lunar terranes from which global properties can be extracted. A similar analogy can be drawn for Earth: unless geophysical information can be drawn across a representative number of terranes on our own planet (e.g., oceanic plates, continents, cratons, plate margins, etc.), it would have been impossible to formulate an accurate geophysical picture of the different internal processes at work within Earth. Indeed, it was shortly after geophysical exploration of the oceanic plates commenced that the paradigm shift to plate tectonics took place. Terrestrial seismology also enables elastic constraints to be related back to mineral properties within the deep interior structure of Earth. Thus, a global network of geophysical stations will enable LGN to fully interrogate the deep interior of the Moon, more accurately locate hypocenters of large moonquakes and impacts, and constrain crustal thickness variations across a wide range of lunar terranes—none of which are possible with the Apollo data.

Electrical conductivity can provide constraints on two key components of the interior, iron and water. These constituents dominate because they are the strongest contributors to lattice defects that foster mobile electrical charges. The Arrhenius relationships favor iron as the highest conductivity at temperatures

>1000–1500 K and water at lower temperatures (see Verhoeven & Vacher 2016 for a review). Because they have different activation energies, the relative contributions of iron and water can be separated along a geotherm. While simultaneous inversion of temperature and composition from electrical conductivity is possible, a more robust result is obtained by combining these data with heat flow, which provides an independent estimate of the geotherm. The joint heat flow and electrical conductivity constraints on temperature and iron/water content can be combined with seismological estimates of temperature and bulk mineralogy for further refinement of the state of the Moon's interior.

The LGN mission will allow more intricate questions to be addressed that have resulted from previous work, such as the following:

1. Do shallow moonquakes (SMQs) represent movement along thrust faults (e.g., Watters et al. 2019)?
2. Do moonquakes present a threat to future human infrastructure (Oberst & Nakamura 1992)?
3. Do deep moonquakes (DMQs) occur on the farside of the Moon (Nakamura et al. 1982; Nakamura 2005)?
4. Is the appearance that the farside is aseismic an artifact of network aperture or interior structure, or is it linked to the presence of maria on the nearside only (e.g., Watters & Johnson 2010; Qin et al. 2012; Laneuville et al. 2018)?
5. What is the mechanism for triggering DMQs (Weber et al. 2009; Kawamura et al. 2017)?
6. Are there global discontinuities in the mantle, and do they relate to the lunar magma ocean (Nakamura et al. 1982; Lognonné et al. 2003)?
7. Do different lunar terranes have unique heat flow budgets, and what does this imply about the bulk geochemical composition of the Moon (Laneuville et al. 2018)?
8. What is the lateral/vertical structure and composition as revealed by electrical conductivity (Hood et al. 1982; Khan et al. 2006a, 2014; Grimm 2013; Shimizu et al. 2013)?
9. What are the differences between nearside and farside hemispheres (e.g., Jolliff et al. 2000)? Are differences observed at the surface manifest in the interior, and if so, how (e.g., Wieczorek & Phillips 2000)?
10. What is the nature of the presumed "partial melt layer" on top of the core–mantle boundary (CMB), and why does it exist (e.g., Elkins-Tanton et al. 2002; Weber et al. 2011; Khan et al. 2014)?
11. Can brittle failure occur at depths where the mantle should be hot (e.g., Khan & Mosegaard 2002; Nimmo et al. 2012; Khan et al. 2013; Kawamura et al. 2017)?

Several lines of evidence indicate that the lunar mantle likely preserves a vertical compositional gradient and at least one internal discontinuity. A whole-moon magma ocean seems most consistent with rapid accretion following the giant impact. Therefore, the boundary between the first two generations of cumulates (olivine versus pyroxene dominated) would lie at a depth between 450 km (Snyder et al. 1992) and 700 km (Elkins-Tanton et al. 2011). Mantle overturn would erase this boundary. Nonetheless, a contrast reappears at 700 km depth in the model of Elkins-Tanton and colleagues. Basaltic mare eruptions represent a later phase of magmatism whose source depths increased from ~150 to >500 km over the interval 4.3–1.2 Ga (e.g., Longhi et al. 1974; Walker et al. 1975; Longhi 1992, 1993; Hiesinger et al. 2011a; Barr & Grove 2013), probably due to global cooling and thickening of the lithosphere (e.g., Snyder et al. 1992). A compositional contrast would be left at the base of the mare basalt source region; however, it is not required by the geophysics (Khan et al. 2006b). Again, mantle overturn may have disrupted initial layering below the floatation crust, but the upper few hundred kilometers may still hold compositionally distinct materials, including sources of the Mg suite.

The discovery of the compositional asymmetry of the Moon (Jolliff et al. 2000 and companion papers) calls into question whether the derived dynamics and petrological structure are truly global or are instead regional specific to that part of the nearside sampled by Apollo. The gamma-ray instrument on Lunar Prospector (LP) revealed that thorium is concentrated on the northwestern nearside of the Moon, as well as, by inference, other incompatible elements that make up KREEP (potassium, rare-earth elements, and phosphorus). The anomalous region encompasses Oceanus Procellarum, Mare Imbrium, and adjacent mare and highlands and so was named the Procellarum KREEP Terrane, or PKT. The rest of the Moon is classified as the Feldspathic Highlands Terrane (FHT), with the exception of the South Pole–Aitken Basin (SPA). While comprising only one-sixth of the Moon's surface, PKT contains nearly two-thirds of the maria area (as well as the youngest mare basalt fields; Hiesinger et al. 2011a) and therefore strongly suggests a connection between KREEP and melting of mare source regions (Wieczorek & Phillips 2000). Korotev (2000) linked certain mafic impact-melt breccias (i.e., "Low-K Fra Mauro" or "LKFM"), and ultimately the entire Mg suite, to KREEP-rich lower-crust and upper-mantle materials that are thus uniquely associated with PKT.

The mechanism by which "urKREEP"—the putative source region for KREEP—was geographically concentrated is uncertain (see Shearer et al. 2006 for a summary). Nonetheless, the distribution of residual urKREEP influences the temperature of the crust and upper mantle, which in turn has implications for the depth and duration of melting, as well as topography and gravity. Wieczorek & Phillips (2000) modeled the thermal evolution of the Moon following emplacement of concentrated, subcrustal urKREEP. They successfully reproduced the differences in heat flow measured at the A15 and 17 sites, and the longevity and depth of melting are well matched to mare basalts. However, such a large thermal anomaly would produce large gravity or topography anomalies that are not observed. Instead, Grimm (2013) found that a similar thermal model in a lower concentration of urKREEP partitioned throughout the crust matched heat flow but damped the mantle thermal anomaly, thus satisfying gravity and topography. While melting depths still exceed 400 km, the duration of melting is reduced compared to the mantle heating case. Finally, the upper 120 km crystallized as a stratified combination of anorthite, oxides, and diverse pyroxenes (Snyder et al. 1992; Elkins-Tanton et al. 2011).

2.2. Science Traceability

LGN's primary goal is to *understand the initial stages of terrestrial planet evolution*. The instruments selected for LGN should have the capabilities required to make the measurements that enable its investigations and objectives and ultimately answer the primary goal. Therefore, to achieve this goal, four *Objectives* explored through six *Investigations* have been identified.

Objectives:

1. Evaluate the interior structure and dynamics of the Moon.
2. Constrain the interior and bulk composition of the Moon.
3. Delineate the vertical and lateral heterogeneities within the interior of the Moon as they relate to surface features and terranes.
4. Evaluate the current seismo-tectonic activity of the Moon (Watters et al. 2015, 2019; Kumar et al. 2016, 2019).

Investigations:

1. Determine the size and state of the core and infer its composition, including the potential for lighter alloying elements (building on the work of Williams et al. 2001; Garcia et al. 2011; Weber et al. 2011).
2. Determine the state and chemical/physical stratification of the lunar mantle (i.e., whether there is garnet in the lower mantle; e.g., Kuskov et al. 2002; Neal 2001; Khan et al. 2006b).
3. Determine the thickness of the lunar crust and characterize its vertical and lateral variability (refining and adding fidelity to the GRAIL results of Wieczorek et al. 2013 and multiplying crustal receiver function analysis; Vinnick et al. 2001).
4. Determine the thermal state of the lunar interior and elucidate the workings of the planetary heat engine.
5. Monitor impacts on the lunar surface as an aid to exploring the lunar interior.
6. Characterize the seismo-tectonic properties at the lunar surface in support of future human infrastructure (e.g., Oberst & Nakamura 1992; Ortiz et al. 2006; Banks et al. 2012, 2020).

2.3. Instrument Performance Requirements

2.3.1. Seismic

Despite being the first digital-feedback seismometer, the Apollo seismometers suffered from their low-resolution acquisition system (10 bit), which was not able to register the instrument self-noise on the Apollo peaked long-period (LP) vertical axis. Although the flat mode was broadband, it was not sensitive enough to capture the low-magnitude DMQs, and most of the Apollo observations were therefore made with the narrowband peaked mode, with a peak sensitivity of about 5×10^{-11} m in displacement or 5×10^{-10} m s^{-2} in acceleration at a period of 2 s (see Lammlein et al. 1974 or the electronic supplement of Nunn et al. 2020 for instrument response curves). Even in this mode the digitization noise remains the main limitation for most of the signals (Figure 2(a)). Many DMQ were therefore recorded with peak-to-peak amplitudes of only a few bits (Bulow et al. 2005; Lognonné & Johnson 2015; Nunn et al. 2020). This leads to partial capture of seismic phases by the lunar seismograms, especially for the core phases, which are expected to be about 10–20 times smaller than the direct P and S phases (Figure 2(b)), and which can be revealed only through stacks (Garcia et al. 2011; Weber et al. 2011). Importantly for future lunar seismic experiments, modeling suggests that the lunar seismic noise may be at least a factor of 10 below the Apollo peaked-mode resolution (Lognonné et al. 2009), which implies that more events will be observed with greater instrument sensitivity.

Following the success of the Seismic Experiment for Interior Structure (SEIS) instrument on InSight (Lognonné et al. 2019, 2020; Giardini et al. 2020) and ongoing development of space qualification for seismic instrumentation (Nunn et al. 2019; Erwin et al. 2020), a sensitivity requirement 10 times better than the Apollo LP sensor can be conservatively achieved for a Very Broad Band (VBB) LGN instrument with a performance level of about 3.5×10^{-11} m s^{-2} Hz$^{-1/2}$ in the LP bandwidth, 0.01–1 Hz frequency range. This sensitivity will allow the detection of core phases (Yamada et al. 2013) for deep interior seismic structure, as well as detection of low-mass meteorite impacts for crustal structure made in conjunction with impact flash monitoring (Yamada et al. 2011). At this sensitivity level, the lander itself will be a source of noise (Panning et al. 2020) and requires active monitoring made with a short-period (SP) seismometer comparable to the SEIS-SP (Lognonné et al. 2019), such as the Silicon Seismic Package (SSP). An additional SP seismometer will be also deployed on the VBB-LGN sensor assembly. With some expected improvement in an SP-like seismometer when tuned for lunar operation (Nunn et al. 2019), a noise floor comparable to (or within a factor of a few above the) Apollo peaked-mode sensitivity can be achieved. The addition of this SP sensor provides some redundancy for the VBB sensor, as well as improving capabilities via combination of six seismic sensors to obtain translational and rotational information (Sollberger et al. 2016; Fayon et al. 2018) of the SP wavefield generated by thermal moonquakes.

2.3.2. Geodetic

Earth-based Lunar Laser Ranging Observatories (LLRO) were first developed in the 1960s to send short laser pulses toward the Apollo retroreflector arrays on the lunar surface, where the Cube Corner Retroreflectors (CCRs) reflected the laser pulses directly back to the LLRO. By highly accurate timing of light-travel time, the distance to the Apollo retroreflector array was determined to centimeter scale, that is, to better than 1 part in 10^{12}. LLR has continued over the past 50 yr, and the analyses of these data have illuminated key details within lunar geophysics, including detecting: the existence and shape of the liquid core, an oblate spheroid with the short axis parallel to the rotation axis of the Moon (Williams et al. 2009); the k_2 Love number and tidal Qs (Williams & Boggs 2015); CMB dissipation (Williams et al. 2001, 2014); active or geologically recent stimulation of rotation normal modes (Eckhardt 1993; Newhall & Williams 1997; Chapront et al. 1999; Rambaux & Williams 2011), improving lunar cartographic networks (with submeter accuracy at the five Apollo reflectors; Williams et al. 1996, 2013; Wagner et al. 2017), as well as providing a check on altimetry from orbit (Fok et al. 2011). In addition, LLR provides the best tests of general relativity and gravitation, improving observations of the strong and weak equivalence principles (Williams et al. 2004, 2012), including providing the only test that measures properties of the gravitational binding energy and the nonlinear effects of gravitational self-interaction (Hofmann & Müller 2018), and providing the best limits on the temporal change in gravitational constant (Williams et al. 2004).

Due to the combination of the design of the Apollo retroreflector arrays and the lunar librations, the uncertainty or jitter in a single range measurement is about 67 mm. The use of the large single solid CCR incorporated in the NGLR will improve the normal point accuracy by a factor of 10 or more,

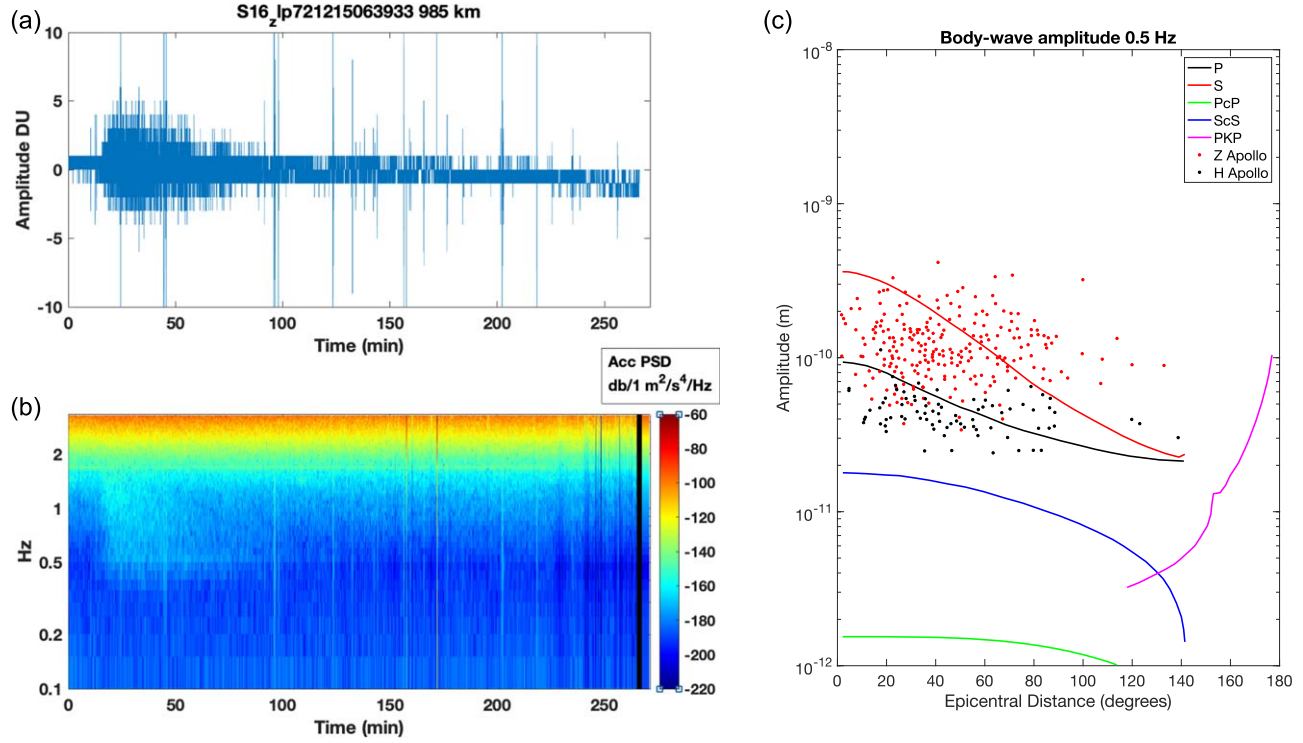

Figure 2. (a) The impact of the A16 ascent vehicle recorded on the A16 LP seismometer. The digitization of the instrument is clearly visible as integer steps in the waveform. (b) A spectrogram, in acceleration power spectral amplitude, shows the spectral content and limitation of the 10-bit acquisition noise, shown in the final section of the spectrogram, after the black line. This 10-bit dynamic range also hinders the identification of seismic arrivals in the frequency domain. (c) LGN's amplitude sensitivity will be a factor of 10 better than Apollo, as well as capturing a larger epicentral distance, enabling core phases to be resolved (e.g., core-reflected shear wave, ScS, core-traversing P-wave, PKP, core-reflected P-wave, PcP) on single records, in contrast to Apollo, which detected only direct P and S phases (Yamada et al. 2013). Red and black points are P and S phases observed from Apollo records, while the expected core phases were all below the instrument resolution and required stacking to detect. Theoretical amplitudes of body waves (color lines) are shown for DMQs as a function of epicentral distance.

leading to the concomitant improvement in the accuracy of the science results for the LGN NGLR array, in particular, these tests include the weak equivalence principle and the inertial properties of gravitational energy, the strong equivalence principle and the spatial and temporal variation of the gravitational constant. To obtain the full accuracy supported by the NGLR instruments, upgrades will be required at the LLRO. Williams et al. (2020) performed simulations that showed that the LLR science results (e.g., beta and gamma of the parameterized post-Newtonian in general relativity and the Love Numbers) using the NGLRs will be several hundred times more accurate than those obtained with Apollo arrays as the LLRO operations and computer modeling improve. The aforementioned science results obtained using the Apollo arrays have already provided the best accuracy currently available. The current NGLR design will provide a return signal at the LLRO that is greater than the current return signal level at the A11 CCR. Moreover, the A11 retroreflector array, which has been sufficient for all of the current LLRO, is known to be dust compromised, which reduces the signal strength but has little impact on range measurements. In the future, we expect that there will be similar dust deposition on NGLR. However, the laser technology is improving far more rapidly than the anticipated dust accumulation. The accuracy of the Apollo science results depended critically on the ability to obtain accurate range measurements over a long duration, i.e., many decades. It is essential that the NGLR be constructed on these demonstrated principles to ensure a long-duration mission, well over 50 yr.

Expanding the current laser ranging network on the Moon through the deployment of NGLR will yield new insights into the Moon and its properties and enhance our understanding of gravitation and of the accuracy of general relativity. Section 3.4 further describes expected NGLR science improvements that are up to hundreds of times more accurate than those obtained with existing retroreflector arrays. In many cases, the latter are already the most accurate results available.

2.3.3. Heat Flow

A heat flow probe makes two separate measurements of thermal gradient and thermal conductivity of the depth interval of the regolith penetrated. Heat flow is obtained as a product of these two measurements. The thermal gradient is obtained by measuring temperatures at multiple depths. The thermal conductivity is obtained in situ by applying heat into the regolith and monitoring the rate of temperature increase (de Vries & Peck 1958). In order to sense the flow of heat originating from the deep interior of the Moon, the probe must penetrate 2–3 m into the regolith, well below the reach of the thermal waves associated with annual and diurnal insolation cycles (Cohen et al. 2009).

The astronauts on A15 and 17 successfully obtained heat flow measurements by drilling holes into the regolith, using a rotary-percussive drill and inserting thermal sensors (Langseth et al. 1976). However, each of these sites was close to the PKT boundary, so an unambiguous heat measurement of the PKT and the FHT was not made. Deploying a heat flow probe semiautonomously on a robotic lander mission such as the

Table 1
LGN Landing Site Requirements

Overarching Criteria	Landing Site Requirements	
	Broader Coverage than Apollo	
	Low-risk Landing Sites (i.e., Low Boulder and Crater Density)	
Measurement Type	Primary	Secondary
Seismicity	Use known seismic sources to examine the core, mantle, and crust	Proximity to thrust faults (lobate scarps, wrinkle ridges)
Laser retroreflectometry	Three nearside stations	Place nearside stations near as possible to the limb
Magnetotelluric	Location well within terrane boundaries	Benign magnetic signature at the surface
Heat flow	Location well within terrane boundaries	Regolith available for full deployment

LGN would require a more compact system with less operational complexity. Such a system is currently under development (Nagihara et al. 2020). This system uses a pneumatic drill in penetrating into lunar regolith, which is more robust than the internal hammering technique employed for the heat flow probe on the InSight mission (Spohn et al. 2018). It integrates the thermal sensors into a pneumatic drill. As the probe penetrates into the regolith, it stops at multiple depths to make the thermal measurements on the way down to 3 m depth.

2.3.4. Electromagnetic

EM sounding recovers the electrical conductivity structure of the interior. Electrical conductivity is a strong function of temperature and, in the absence of free water, depends on composition-dependent ionic charge defects that for the Moon are most likely due to the abundance of ferric iron or hydrogen. EM sounding is complementary to measuring heat flow, in that the latter provides a boundary condition on the temperature profile derived from the former.

EM sounding was successfully performed during Apollo using the magnetic transfer function (TF), which compares the magnetic field at the target (the sum of source and induced fields) to a known, distant source field (see Sonett 1982 for a review). These two quantities were measured by magnetometers at the A12 lunar surface site and the orbiting Explorer 35 satellite, respectively. Different formulations were used depending on whether the magnetometer and Moon were in the dayside solar wind (Sonett et al. 1972), Earth's magnetotail (Hood & Schubert 1978), or the lunar wake (Dyal et al. 1972). There was variation in the inferred temperature–depth curves: The first approach was consistent with thermal models for the Moon showing contemporary lower-mantle subsolidus convection (Hood & Sonett 1982; Khan et al. 2006a). However, higher conductivities obtained in the last approach could require substantial internal melting. The A12 site was in the middle of PKT, calling into question whether its electrical conductivity profile is representative of the bulk Moon (Grimm 2013). A distribution of LGN magnetometers across PKT and FHT, together with an orbital reference measurement, would resolve differences in the principal terranes, as well as providing global properties.

LGN can, however, exploit an alternative method that will yield more robust and better-resolved results, without requiring a reference orbiter. In the MT method, electrical conductivity structure is determined by simultaneous measurement of the electric and magnetic fields at a single site (e.g., Simpson & Bahr 2005; Chave & Jones 2012). By eliminating the orbital measurement, data can be interpreted consistently across all three environments described above. Furthermore, MT is largely insensitive to finite wavelengths in the plasma that introduce distortions in the TF at frequencies of tens of mHz and higher (Grimm & Delory 2012). A larger bandwidth enables resolution of shallower structure than previously, particularly if the traditional fluxgate magnetometer is complemented with a search coil magnetometer. The system of surface electrodes used to measure the electric field is similar to those used in space physics (e.g., Bonnell et al. 2008) and naturally has broadband performance. A Lunar Magnetotelluric Sounder (LMS) has been selected for flight under NASA's CLPS program. In order to determine the electrical conductivity to as shallow as 200 km with 20% accuracy, LMS must measure electric and magnetic fields to 10 Hz with resolutions of 6 μV m^{-1} and 90 pT, respectively.

3. Landing Site Science Rationale

The general and measurement-specific criteria for the LGN landing sites are outlined in Table 1. Any landing sites for the LGN mission should greatly expand the footprint of the prior Apollo geophysical network, including the farside, and use the knowledge gained by Apollo about the Moon to strategically investigate the nature of the lunar interior. A wider geographical spread of stations permits improved global structure determination from seismology and laser ranging. Including a station near the lunar limb, the edge of the visible disk of the lunar nearside hemisphere, maximizes the geographical extent between stations. The farside station will optimize new assessments of global seismicity and the structure of the Moon's lower mantle and core (see Section 3.3.2). The stations should maximize the recording of seismic signals from known DMQ clusters as they pass through the lowermost mantle and core (Figures 3 and 4; Yamada et al. 2013), and they should expand the current LLR network (Figure 1). They should also be well within terrane boundaries to unambiguously make MT and heat flow measurements both inside and well outside the boundaries of the PKT. Secondarily, landing sites should (1) be in the proximity of recently recognized thrust faults (lobate scarps) that could still be active and represent sources of SMQs (e.g., Kumar et al. 2016, 2019; Watters et al. 2019), (2) avoid local crustal magnetic anomalies that would contaminate the MT sounding measurements, and (3) be on surfaces of sufficient age such that the regolith is suitably developed to allow the full deployment of the heat flow probe. Regolith thicknesses vary widely with generally thicker regolith on the farside and thicker regolith in the highlands versus the maria (e.g., Bart et al. 2011). Assessing an average rate of regolith formation will yield a rough order-of-magnitude estimate at best but is needed for planning purposes. Regolith formation and overturn are dependent on crater flux, the influence of

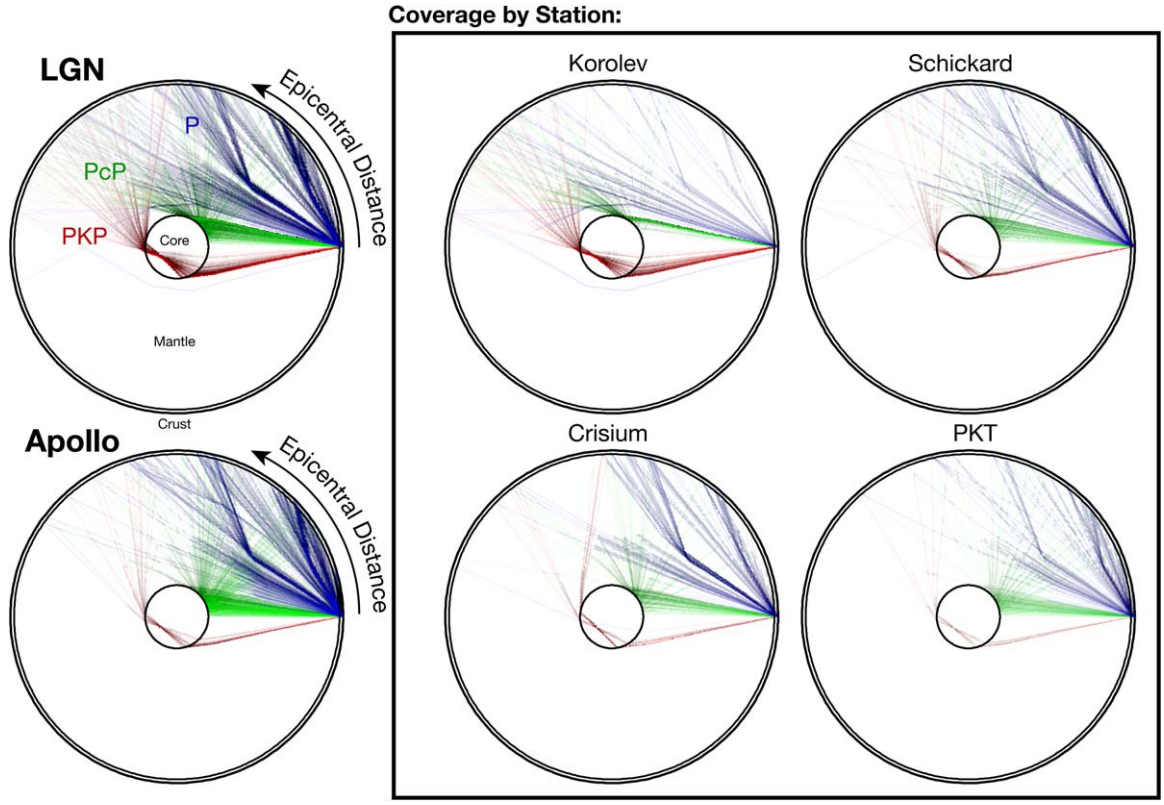

Figure 3. Ray path coverage for P (blue), PcP (green), and PKP (red) phases from the known distribution of DMQ clusters, rotated such that the station is fixed at 0° and stacking all stations in the array for LGN (top left) and Apollo (bottom left). Note LGN's wider coverage in epicentral distance and the denser sampling of the deep interior. The box on the right shows ray coverage for each of the LGN stations separately.

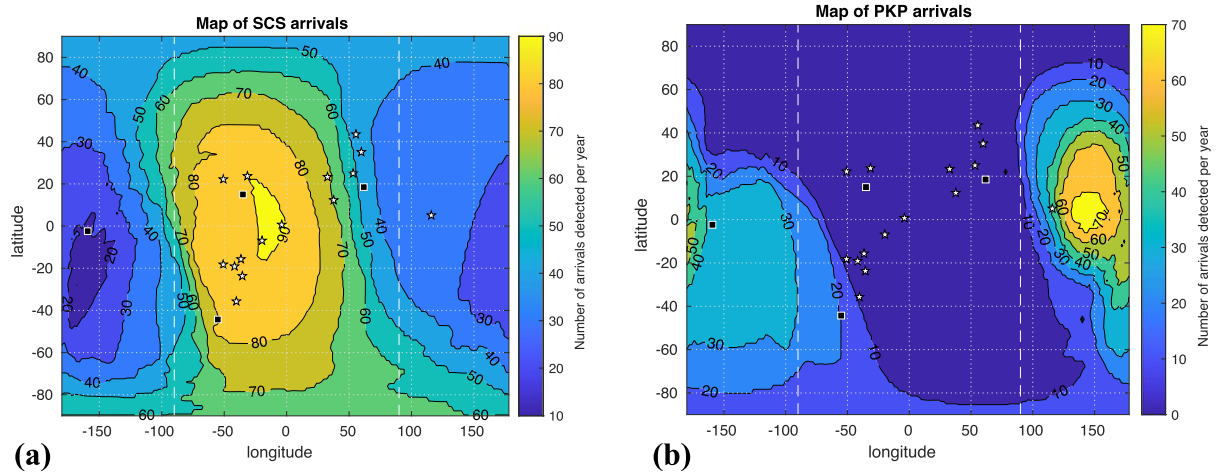

Figure 4. (a) Number of core-reflected shear-wave (ScS) phases and (b) number of core-traversing P-wave (PKP) phases detected per year (color bar) from 15 energetic DMQ nest epicenters (white stars) as a function of the location of a VBB seismometer. Black squares indicate LGN station locations. The numbers of (ScS; PKP) core phases detected at these positions are (87; 2), (78; 20), (45; 0), and (17; 35) for PKT, Schickard, Crisium, and Korolev stations, respectively. Vertical dashed lines mark the limit between farside and nearside. Computed for an rms noise level of 1.49e−11 m s^{-1} in the 0.07–0.14 Hz frequency range following the method described in Yamada et al. (2013).

secondary impacts, and the size of the impact (Costello et al. 2018). Various authors estimated regolith formation on the order of ∼3–5 mm of new regolith per million years at ∼3.8 Ga and about 1 mm Myr^{-1} from ∼3.5 Ga to the present day (Oberbeck & Quaide 1968; Quaide & Oberbeck 1968, 1975; Hörz et al. 1991; Fa et al. 2014; Costello et al. 2018, 2020; Hirabayashi et al. 2018; Yue et al. 2019). This equates to 1 m of regolith formation per billion years. In order to facilitate heat flow probe deployment up to 3 m, a landing site on a surface ⩾3 Ga is needed.

3.1. Landing Site Examples

For the purposes of this paper, we have applied the landing site criteria (Table 1) to achieving the goal of the LGN mission. Therefore, example landing sites have been chosen to reflect a

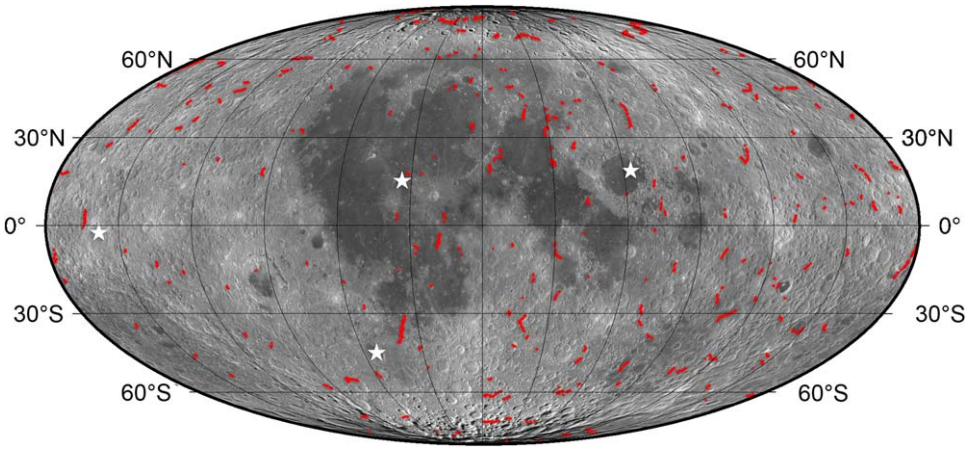

Figure 5. Global distribution of lunar lobate scarps. These lobate thrust fault scarps (red lines) are found predominantly in the highlands, at all latitudes. Over 3500 of these young fault scarps have been detected thus far in LROC images. LGN proposed stations are marked (stars).

global distribution around the Moon, greatly increasing the footprint of the former Apollo network (Figure 1). Four landers are baselined, three on the nearside and one on the farside, with the sites chosen to fulfill the landing site criteria described above (Table 1). Rationale for these example sites are as follows:

Procellarum KREEP Terrane (P-5 basalt field; Hiesinger et al. 2003) site southeast of the Aristarchus Plateau (latitude = 14.°9; longitude = −35.°5): Relatively flat volcanic terrain with few craters and boulders that has a crater size–frequency distribution age of 3.48 Ga (Hiesinger et al. 2011a). This landing site is well within the boundaries of the PKT and close to the Th high just west of Copernicus crater (Figure 1). It is situated on basalts of sufficient age and with sufficient available regolith for full deployment of the heat flow probe. This example site is well situated to detect both direct and core-reflected arrivals from the known nearside DMQ clusters (Figure 4). Lobate scarps are in this region to the east and southeast of this site (Figure 5).

Schickard Basin (latitude = −44.°3; longitude = −55.°1): This site is in the southern hemisphere of the Moon, and the floor is partially flooded with basaltic lava flows (3.62–3.75 Ga; Hiesinger et al. 2011a) that form a relatively flat landing site, with few craters and boulder fields, but are old enough to have regolith thicknesses that allow full deployment of the heat flow probe. This example site is well outside the PKT, situated ideally to detect seismic phases reflected by the lunar core by known DMQ clusters in the northeastern quadrant of the nearside and refracted waves from the farside A-33 DMQ cluster through the core (Figure 3). It does not contain any local magnetic anomalies. Lobate scarps are in the region around the Schickard Basin (Figure 5). This example site also expands the LLR network into the southern hemisphere of the Moon.

Crisium Basin (latitude = 18.°5; longitude = 61.°8): The basaltic lavas on the floor of the basin form a relatively flat terrain but contain secondary crater populations that will need to be avoided. According to the latest crustal thickness maps, the primary crust is essentially absent (Wieczorek et al. 2013), allowing mantle heat flow to be directly measured. Seismic measurements of the mantle at this site will also benefit from not being distorted by the fractured crust. For MT measurements, the known magnetic anomalies within Mare Crisium (e.g., Richmond & Hood 2008) need to be avoided. Therefore, this site is in the northeast section of the basin, where the age of the basalts (based on crater size–frequency distributions) is 3.2 Ga, although a 2.5 Ga unit is observed in the extreme northeastern sector of Mare Crisium (Boyce & Johnson 1977; Hiesinger et al. 2011b). Note that Luna 24 returned basalts that yielded an age of ∼3.65 Ga based on Rb-Sr systematics (Nyquist et al. 1978). This site is located close to wrinkle ridges within Mare Crisium, and lobate scarps are located in the south of the basin and just to the east (Figure 5). This example site also expands the LLR network farther to the east.

Korolev Basin (latitude = −2.°4; longitude = −159.°3): This site will allow the first surface geophysical measurements to be made on the farside of the Moon. The Korolev Basin is a Nectarian-age basin (3.85–3.92 Ga) and affords a relatively flat and boulder-free landing area that is in the vicinity of a lobate scarp. It is situated well within the FHT and in the highest topographic area of the Moon, which represents the thickest crust (see Wieczorek et al. 2013). The site is approximately antipodal to many nearside DMQ clusters, again improving ray coverage for core-traversing seismic phases (Figure 4 and Yamada et al. 2013). This site will contain sufficient regolith for heat flow probe deployment and does not contain any local magnetic anomalies. A lobate scarp is close to the western margin of the basin (Figure 5).

3.2. Landing Site Descope Options

While the *baseline* LGN mission is for four identical landers to be distributed around the Moon, the *threshold* mission is for two landers: one at the PKT (P-5) site and one in the Schickard Basin (Figure 1). This preserves deployment in distinct terranes with distinct crustal thicknesses and thermal regimes, uses known DMQ clusters (including those on the farside) to explore the deep lunar structure, and expands the current LLR network. Between the baseline and threshold missions a graceful descope trade space exists. The lander descope scenario presented here places the farside site as a high priority, as this maximally enables observation of core-transmitted phases from the known nearside DMQ clusters (Yamada et al. 2013).

1. Descope the Crisium lander. Rationale: minimizes impacts to observations of seismic coverage for core-transmitted phases. Crisium Basin will have some geophysical data from the 2023 CLPS mission, although no seismic data will be returned. Removal of this site also

removes expansion of the LLR network to the eastern part of the Moon.
2. Descope two nearside landers (Schickard and Crisium). Rationale: minimizes impacts to observations of seismic coverage for core-transmitted phases, and preserves deployment of landers in the PKT and the farside FHT. The remaining two sites permit using DMQ activity to explore the core and mantle of the Moon (the Korolev Basin site is antipodal to the nearside A-1 DMQ nest, and the PKT site is offset to the A-33 farside nest to explore mantle structure).
3. Descope the communications satellite and deploy four nearside landers. Rationale: reduces operational complexity, but has direct to Earth as the only communications option. Place the original farside lander at a polar region (e.g., in the Wiechert region of the south pole close to the observed lobate scarps). This removes any investigation of the thick crust on the farside but retains the investigation of lobate scarps and heat flow in the FHT and adds an NGLR station at the south pole.
4. Descope the orbiter and farside lander, deploy three nearside landers in the sites proposed. Rationale: reduces operational complexity, but has direct to Earth as the only communications option.
5. Descope the Crisium and Korolev landers and the communications satellite. Rationale: this represents the threshold LGN mission. This preserves the ability to understand the internal structure of the Moon (utilizing DMQ cluster activity), records heat flow within the PKT and FHT, adds a southern hemisphere node to the NGLR network, and thus achieves the LGN mission goal.

3.3. Seismic Network Requirements

3.3.1. Seismic Ray Density

The geometry of the seismic array is the predominant driver for LGN site selections. The LGN stations are situated to vastly improve our knowledge about the lunar deep mantle and core. Compared to Apollo, the wider aperture of the LGN array and geographical distribution of the stations provides ray path sampling of the entirety of the lunar interior. Using the seismicity catalog of Apollo, we calculated ray path densities for P (direct compression wave), PcP (core-reflected P-wave), and PKP (core-traversing P-wave) to the LGN across epicentral distances using the Weber et al. (2011) velocity model and proposed LGN station locations (Figure 3). Consistent seismic ray path density across epicentral distance is crucial for providing a full picture of lunar internal structure. The LGN provides a significantly denser sampling for core-traversing waves (e.g., PKP), waves that sample the deep mantle (PcP, P), and more uniform sampling of the crust and upper mantle than Apollo. The more complete coverage is enabled by the deployment of four stations, particularly from a farside station in Korolev crater that provides deep mantle and core sampling and will allow for the detection of farside seismicity that was unobserved by Apollo.

Ray path density through depth in the lunar interior is obtained by taking event hypocenters from Gagnepain-Beyneix et al. (2006) and ray-tracing to the locations of both the LGN stations (Figure 1) and the Apollo stations for comparison. Ray paths are calculated assuming the Weber et al. (2011) velocity model using the TauP Toolkit (Crotwell et al. 1999) for all sources and the phases P, PcP (core reflections), and PKP (core traversals). Each event/station pair is aligned on the great circle path and arranged by epicentral distance from individual stations to illustrate sampling density with depth (not accounting for 3D sampling geometry). Apollo stations primarily sampled the uppermost mantle and crust of the Moon. By comparison, the LGN station geometry, assuming similar seismicity, would provide at least double the increased sampling density within the core and lowermost mantle and extend sampling to rays traversing to greater epicentral distance.

To quantify LGN's increased coverage at a given distance, consider the observed distribution of events of the Apollo event catalog. Ray paths that are sensitive to PKP range from 180° to 270°. For PKP, LGN will observe 100% of events at these distances with at least one event per 5°, whereas the Apollo Passive Seismic Experiment only had 55%. LGN covers 89% of these distances with two or more events per 5° and 72% for three or more events per 5°. In contrast, Apollo covered only 16% for two or more events and 11% (using one small distance window of ±5°) for three or more. LGN expands the distance range covered by the Apollo network to a truly global sampling of ray paths. This is a conservative estimate assuming that LGN were only to record the distribution of seismicity seen by Apollo; however, extrapolating to a larger collection area and improved instrument sensitivity will improve ray coverage statistics. The long-term periodicity of the DMQ clusters has been determined to still be active today (Weber et al. 2010).

3.3.2. Location Optimization for Deep Structure Determination

Previous work suggests that networks with large distances between stations provide the best configurations for deep structure determination, including the core (Yamada et al. 2011). Accordingly, the mean distance between the stations of the notional LGN network is therefore around 105°, including a station on the lunar farside. The farside station serves two additional purposes: first, it permits detection of farside seismicity, which was seldom observed by the nearside Apollo array (Nakamura 2005); and second, it increases detectability of secondary seismic phases from the known distribution of DMQ clusters that traverse the core (Figure 4). To discriminate between these core phases and the direct P-wave arrival, the farside station should be located far from the lunar limbs. The Korolev station location is consistent with these requirements.

The nearside stations are closer to the limbs, which will permit the detection of direct P waves from meteoroid impacts. These occur preferentially closer to the leading limb (Le Feuvre & Wieczorek 2011) and are observed at both limbs by the ground-based impact flash monitoring program (Moser et al. 2015). These impact flash detections provide a reference timing and location for the events recorded on the seismometers and will provide strong constraints on estimates of crustal structure around these stations.

Core phase detection is illustrated in Figure 4 (adapted from Yamada et al. 2013), which shows the number of ScS (core-reflected shear wave) and PKP phases detected per year at 0.1 Hz by a VBB instrument with noise specifications indicated in Section 2.3.1 ($3.5e{-}11\ m/s/s/\sqrt{Hz}$ at 0.1 Hz), from 15 of the most active DMQ nests. This computation takes into account the number of events per year at each nest and the distribution of their moment magnitudes as measured by the Apollo network (see Yamada et al. 2013) and assumes the Very Preliminary REference MOON model (VPREMOON) seismic

velocity and attenuation model (Garcia et al. 2011). The maximum ground velocity of each phase is computed at 0.1 Hz, and a detection is counted when this value is five times larger than the rms instrument noise in the 0.07–0.14 Hz range, which is estimated to be 1.49e−11 m s^{-1}. Due to the refocusing of seismic waves at the antipode of their source, seismic events with the lowest seismic moment allow PKP detections only at their antipode, whereas larger seismic moments allow detections over a large epicentral distance range. These numbers represent a lower bound because additional detections may be performed from quakes already located by Apollo but observed with a higher signal-to-noise ratio by LGN, as well as newly detected quakes located only by LGN stations.

The stations on the nearside are located to adequately detect ScS phases from already-known DMQ locations. The farside Korolev crater location is situated among the antipodes of a high number of nearside DMQs, thus optimizing the number of PKP phase detections over a large epicentral distance range. The uncertainties on the DMQ moment magnitude translate into an error bar on the optimized locations of seismometers of at least 5°. The LGN sites are positioned to capture the required minimum of at least one path for core-traversing PKP seismic waves generated by an Apollo-detected DMQ cluster, and they also provide a chance to see PKP over a range of distances that will enable determination of core velocity structure and layering. Note that the farside Korolev station, in the event that it detects farside seismicity, will also be able to record core-reflected phases from that seismicity.

3.3.3. Lobate Scarps

It has long been held that lunar tectonics, the deformation of the Moon's near-surface crustal materials, was largely restricted to the mare basins, and that this deformation was ancient. This view has been radically altered by high-resolution Lunar Reconnaissance Orbiter Camera (LROC) images collected over the past decade. A globally distributed population of lobate scarps has been revealed in these images (Figure 5; Watters et al. 2010, 2015, 2019). Lunar lobate scarps are small-scale landforms that are the surface expression of thrust faults, contractional faults that displace crustal materials up and over adjacent terrains (Binder 1982; Watters & Johnson 2010). Even more remarkable is the age of these fault scarps, indicated by their small size, pristine appearance, lack of superimposed impact craters, and cross-cutting relations with small-diameter craters—all suggesting that they are very young (Watters et al. 2010). The size–frequency distributions of impact craters proximal to the scarps and erasure of crater populations $<\sim$20–100 m in diameter up to kilometers away show that the fault scarps were actively forming in the late Copernican (<400 Ma; van der Bogert et al. 2018). A very young age is also estimated from infilling rates for small-scale back-scarp graben, suggesting that the fault scarps were active within the past 50 Ma (Watters et al. 2012; Kumar et al. 2019).

To date, over 3500 lobate scarps have been identified on the Moon (Watters et al. 2019; Figure 5). Although they occur in both the highlands and mare terrains, they are most commonly found in the highlands, where they are the dominant tectonic landform. The large number of fault scarps, their global spatial distribution, and their very young age have led to the hypothesis that the faults are currently active and could be the source of some moonquakes recorded by the Apollo Seismic Network. Twenty-eight SMQs, with hypocenter depths generally constrained to be <100 km, are among the strongest recorded events (Nakamura et al. 1979; Khan et al. 2000; Gillet et al. 2017). Contrary to this previous work, Watters et al. (2019) postulate a much shallower origin for SMQs (<1 km). A comparison of relocated candidate epicenters with surface solutions only, generated by an algorithm adapted for sparse seismic networks, indicates that 8 out of 17 SMQs with surface solutions fall within 30 km of a mapped lobate scarp (10 inside of 60 km), the closest within 4 km (Watters et al. 2019). Shake models predict moderate to strong ground shaking over a distance of 30–60 km (Watters et al. 2019). In addition, seven SMQs within 60 km of a lobate scarp occur near the regions where stress models predict peak compressional stresses (Watters et al. 2019). The proximity and timing of SMQs support the hypothesis that they are due to slip events on lobate scarp-related active thrust faults.

Additional criteria for selecting the locations of the LGN landing sites are their proximity to potentially active faults (see Table 1). The nominal PKT site is ∼460 km from one of the most prominent lobate scarps found in mare basalts. The Herodotus scarp (informal name) occurs near the southern margin of the Aristarchus Plateau and has a maximum relief of ∼100 m. The site is also ∼110 km from a wrinkle ridge–lobate scarp transition in Procellarum. These transitions occur at the contact between mare basalt and highlands or highland massifs and reflect the response of the thrust fault to the contrast in mechanical properties (Watters & Johnson 2010). The highlands within ∼500 km of the Schickard Basin landing site have a large number of lobate scarps and scarp clusters. This includes the Vitello cluster, one of the longest clusters of lobate scarps found on the Moon. The closest lobate scarp is on the western rim of Schickard, ∼90 km from the nominal landing site. The Mare Crisium landing site is dominated by wrinkle ridges. However, on the southern margin of Crisium, a wrinkle ridge–lobate scarp transition is found ∼250 km from the proposed landing site. The Korolev Basin landing site is near another large cluster of lobate scarps. Outside the northwest rim, ∼180 km from the nominal landing site, is the Korolev cluster. This prominent cluster of scarps covers over 140 km of terrain. Thus, the proposed LGN landing sites are well placed to detect coseismic slip events on lobate scarp thrust faults.

3.4. Geodetic Station Optimization

To understand the expected science return of an NGLR network, we performed simulations with varied number of stations and LLRO measurement precision. These results are compared to the Apollo CCR array for a variety of science parameters, and factors of accuracy improvement are tabulated in Table 2. Six years of synthetic LLR data from the network of proposed nearside sites are considered. We assume the use of the current range accuracies for the Apollo retroreflector arrays. The accuracy of a normal point, which requires multiple ranges, obtained by the LLRO depends on the hardware and observing procedures at that location.

The first row considers the improvement in the accuracy with respect to the LLR accuracy obtained with the current retroreflectors under the assumptions of the three NGLR and LLRO normal point accuracies of 1.5 mm. Precision at this level has already been obtained at the Apache Point Observatory Lunar Laser-ranging Operation (APOLLO) LLRO. The second row addresses the improvement in the factors when a fourth

Table 2
NGLR Simulated Accuracy Improvement over Current for Three and Four Nearside Locations, Seven Science Parameters, and at 1.5 or 0.15 mm LLRO Normal Points Precision

No. of Sites	Accuracy	Beta	Gam	h_2	l_2	cos D	$<a>$	Tau
3	1.5 mm	4	7.2	5	5	2.8	3.2	3.5
4	1.5 mm	4.4	7.4	6.8	13	3.2	4.2	3.6
3	0.15 mm	100	410	20	27	145	120	31
4	0.15 mm	111	420	212	570	162	147	330

Note. The three nearside locations are the three CLPS landing sites. Four sites include these and the Artemis III site. The science parameters encompass geophysics and astrophysics analyses (as described in text). The simulations assume the LLRO that are currently performing ranging (APOLLO, MeO, Matera, and Wettzell), and their rates of ranging operations. The current NGLR design will support the best accuracy (0.15 mm) showing consistent increase in science return.

NGLR is deployed at the south pole (i.e., the Artemis III site). A second set of simulations (Williams et al. 2020) is shown in the third and fourth rows for three and four NGLRs with range accuracies of 0.15 mm, addressing the limiting accuracy that the NGLR will support in the current design of the LGN deployment. The basic NGLR package can support very high accuracy ranging (Currie et al. 2013). The accuracy improvement for a given science result is estimated for a single range for the basic NGLR package (Currie et al. 2013), with the normal point being obtained by multiple ranges. These results require an upgrade in LLRO hardware. In order to reach the goal of 0.15 mm accuracy, the horizontal gradients of temperature, density, and humidity in Earth's atmosphere must be determined either by modeling or by direct measurement. The modeling approach has been demonstrated using data from a variety of satellite laser ranging stations (Masoumi et al. 2017; Drożdżewski et al. 2019), although it has not yet been implemented at any of the LLRO.

Improved ranging accuracy is achieved by expanding the footprint of LGN's NGLR and translates into improved science results as a function of the number of NGLR deployed (three or four stations) and status of the LLRO. In particular, the landing sites far from the equatorial sub-Earth point, like the example LGN landing sites or a nearly polar site such as the nominal south pole site of the Artemis III mission (longitude = 0, latitude = −88), are considered. The simulations assumed that the NGLR are deployed at Mare Crisium (longitude = 59, latitude = 17), a western site region (longitude = −50, latitude = 20), and a southwestern site (longitude = −55, latitude = −45), which are the sites expected to be explored by missions of the NASA CLPS program with NGLR funded by the NASA Lunar Surface Instrument and Technology Payloads (LSITP) program, and the south pole Artemis III site. We expect the LLR science improvements due to any of the nearside LGN sites to be comparable. If both LGN and CLPS deployments are successful, along with the currently existing retroreflector arrays, the science results will be further improved, particularly the Love Numbers and the selenodetic coordinate system. The latter will improve the accuracy of maps of various properties of the lunar surface, particularly catalogs like that from LRO. Deployments near the limbs and/or the poles, as compared to the current sites, will improve science accuracy by a factor of 3–5.

The science parameters listed in Table 2 include moment combinations $b = (C–A)/B$ and $g = (B–A)/C$, the distortions of the lunar crust in response to the tidal forces (Love Numbers h_2 and l_2), a parameter (cos D) that addresses the general relativistic weak equivalence principle, the total mass of the Earth–Moon system that depends on the mean semimajor axis ($<a>$), and the longitude librations (Tau) at 815 days. All values in Table 2 are positive, indicating improvement over previous ones. The simulations show that similar improvements by factors of hundreds in the science results with respect to the Apollo results can be obtained with the LGN NGLR deployments. This demonstrates the expected high degree of improvement in the accuracy of these science parameters with the LGN NGLR.

The Apollo results are based on ranges obtained from the past and current LLRO (see https://ilrs.gsfc.nasa.gov/network/stations/index.html for global map of stations) ranging to the existing retroreflector arrays (or have contributed significant ranging data in the past). These consist of LLRO located in the US, i.e., McDonald (MCDl; Silverberg & Currie 1971) and (MLRS), Hawaii (Hall) and Apache Point (APOLLO; Murphy et al. 2004), France (MeO; Chabé et al. 2020), Italy (Matera; Varghese et al. 1993), and Germany (Wettzell).

3.5. Heat Flow Observation Considerations

In understanding the Moon's thermal evolution, it is important to quantify the contribution of crustal radiogenic heat to the overall heat budget of the Moon and its geographic variation. The Apollo program considered heat flow measurements a high priority and originally planned to carry out measurements by astronauts on four of the landed missions. However, only two of them (A15 and 17) made successful heat flow measurements (Langseth et al. 1976). Since then, a number of expert panel studies have recommended additional heat flow measurements for future lunar-landing missions (National Research Council 2007; Cohen et al. 2009; National Research Council 2011; Lunar Exploration Analysis Group 2017), because the two existing measurements alone are not sufficient.

The heat flow values obtained by the A15 and 17 astronauts were 21 mW m^{-2} and 16 mW m^{-2}, respectively (Figure 6). It has been hypothesized that the higher value at the A15 site was due to its location being within the PKT with higher concentrations of radionuclides in the crust (Wieczorek & Phillips 2000). To further test this hypothesis, we should examine whether or not surface heat flow values have a positive correlation with the surface abundance of radionuclides. Besides the surface abundance of radionuclides, other factors such as crustal thickness (Figure 7) and lithology may also be controlling the radiogenic heat production within the crust.

We should also acquire a data point in an area where crustal radiogenic heat is expected to be minimal in order to establish a baseline for the Moon. Such a baseline value should closely approximate the heat flow out of the lunar mantle. The mantle heat flow estimate, combined with the MT sounding and the seismic investigation, would enable us to unambiguously constrain the thermal properties and composition of the deep interior of the Moon.

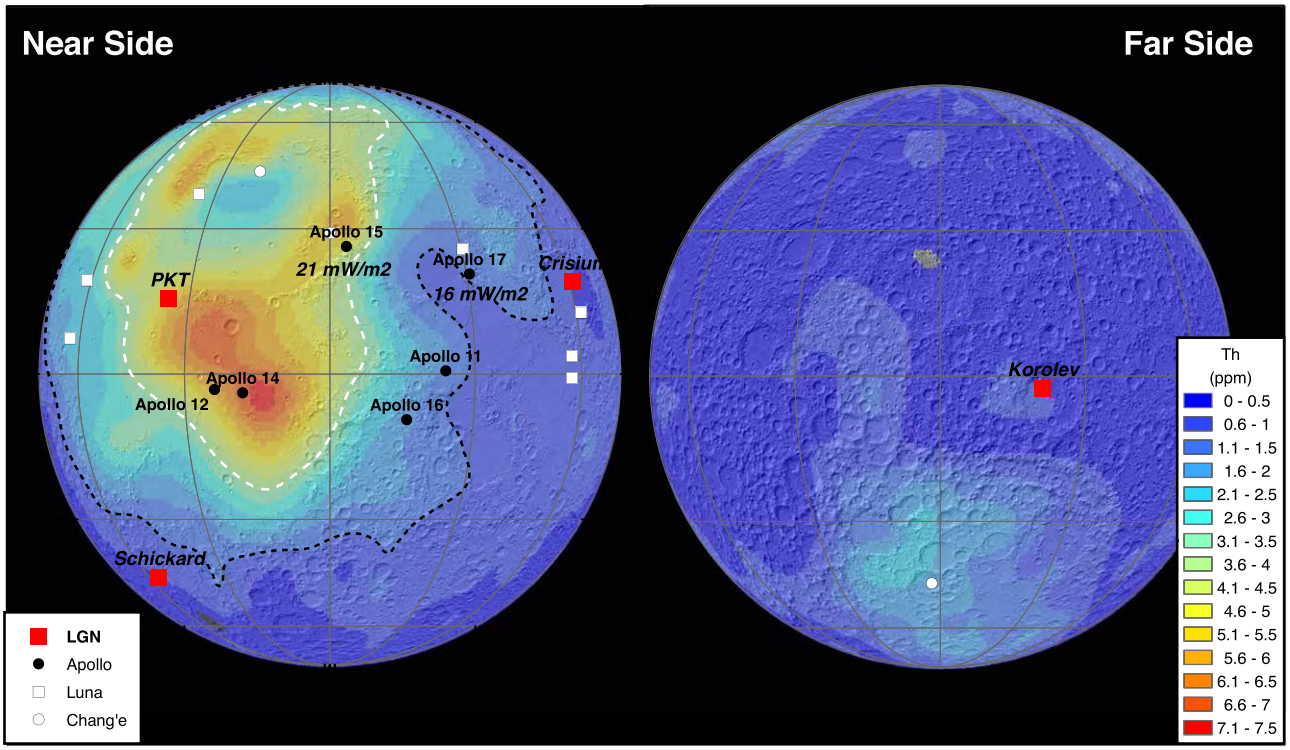

Figure 6. Near- and farside maps of surface thorium concentration (ppm) obtained by the Kaguya mission (https://darts.isas.jaxa.jp/planet/pdap/selene/index.html.en). The red squares indicate the proposed landing sites for the LGN mission. The landing sites for the Apollo, Luna, and Chang'e missions are also shown by circles and squares. The white dashed line is the 3.5 ppm contour and roughly delineates the geographic extent of the PKT. The black dashed line is the 1 ppm contour, which can be used as the minimum geographic extent of the area where heat flow may be affected by Th-rich ejecta from the Imbrium basin-forming impact. The heat flow values at the A15 and 17 sites are also shown.

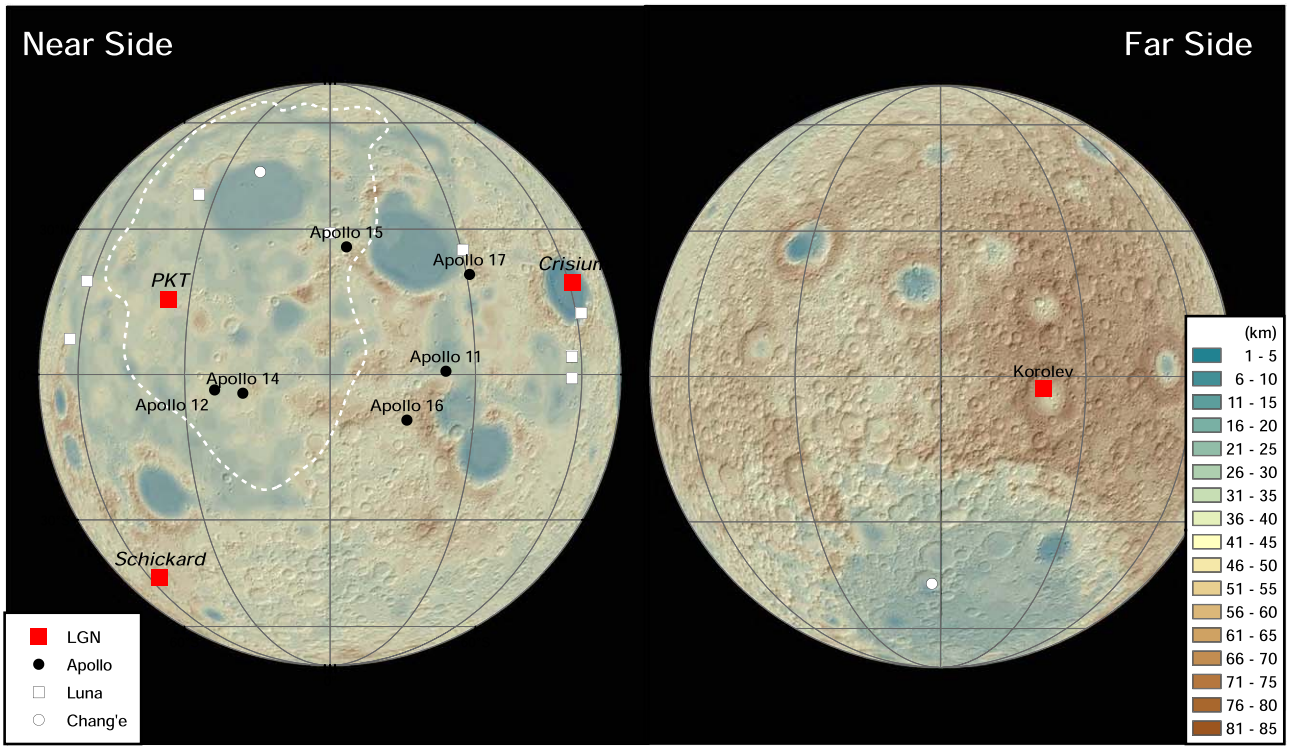

Figure 7. Near- and farside maps based on the crustal thickness estimates (km) obtained by the GRAIL mission (Wieczorek et al. 2013). The red squares indicate the proposed landing sites for the LGN mission. The landing sites for the Apollo, Luna, and Chang'e missions are also shown by circles and squares. The white dashed line is the 3.5 ppm contour and roughly delineates the geographic extent of the PKT.

Table 3
A List of the Criteria and the Remote Sensing Data Used for Landing Site Consideration

Criteria	Instrument[a]	Available Data Set	Spatial Resolution
Wide, smooth, and level surface	SC, S, HF, NGLR	SLDEM (LOLA and Kaguya) LROC-NAC DTM	60 m ∼ 2 m
Regolith thickness > 4 m	HF	Arecibo *P*-band radar	400 m
Fine-grained regolith	HF	Arecibo *P*-band radar Arecibo *S*-band radar LRO-diviner rock abundance	400 m 80 m 240 m
Avoid large (<100 nT) magnetic anomalies	MT	Lunar Prospector, Kaguya-LMAG	1°
Relatively uniform crustal thickness	S, HF, MT	GRAIL	0°.25

Note.
[a] SC: spacecraft; S: seismometer; HF: heat flow probe; NGLR: Next Gen Lunar Retroreflector; MT: magnetotelluric instrument.

The four landing sites proposed for the LGN mission, together with A15 and 17, will allow us to sample a large range of radionuclide concentrations, crustal thickness, and lithology (Figure A1). The "PKT" site and A15 are located within areas of high Th concentration (4.5–5 ppm) with variable crustal thicknesses (25 and 39 km, respectively). "Schickard," "Crisium," and "Korolev" are located far outside of the PKT with very low Th concentrations (0.5 ppm). Crisium has a very thin (<10 km) mare crust, and a heat flow measurement there could establish the baseline for the Moon. Korelev and Schickard have highland crust with 58 and 42 km thick crust, respectively.

3.6. Electromagnetic Network Requirements

Previous EM experiments, performed at Apollo landing sites, were within or adjacent to the PKT. Therefore, it is unknown whether or not the deep electrical conductivity profile derived at A12 (see Sonett 1982 for a review) is representative of the whole Moon. Comparison of sites in both PKT and FHT can test specific hypotheses for the lunar interior described above. If the electrical conductivity is lower beneath the FHT, then additional heat sources indeed likely exist in the PKT upper mantle. If the sub-FHT conductivity is higher than PKT, then there is no anomalous mantle heating, and either the PKT mantle is depleted in Fe or H_2O compared to FHT or the FHT mantle is actually hotter owing to thicker, insulating crust (in spite of likely lower-mantle heat flow).

Additional sites within PKT are also useful. Mare Imbrium is a particularly diagnostic site (Nagihara & Grimm 2020), as its thin crust and low surficial thorium suggest that crustal KREEP was excavated by the basin-forming impact. If the heat flow is comparable to the A15 measurement, then a mantle heat source is confirmed and the crustal geochemical signature is only incidental to thermal evolution. Conversely, significantly lower heat flow would point to the dominance of crustal radioactivity. In both cases, the electrical conductivity profile can be anchored on the heat flow measurement to discern and compare upper-mantle temperatures.

4. Mare Crisium Detailed Site Survey—Case Study

We illustrate the details of site selection within the Mare Crisium Basin, with emphasis on the requirements primarily from heat flow and EM sounding. Mare Crisium is desirable because it not only is outside of PKT but also lies on a great circle from the middle of PKT through the A15 and 17 sites, where heat flow was previously measured. Furthermore, Mare Crisium is underlain by some of the thinnest crust on the Moon, so the heat flow signature there will be representative of the bulk Moon, which can be linked along a great circle back into the PKT. On the basis of these factors advocated by the Lunar Instrumentation for Subsurface Thermal Exploration with Rapidity (LISTER) and LMS teams, Mare Crisium has been selected for the CLPS 19D mission landing site (with other payloads that are site agnostic). This site for use within the LGN network will be reevaluated following a successful CLPS 19D mission in the 2023 time frame. Heat flow, magnetotellurics, and NGLR would all benefit from observing different locations than previous sites.

Other criteria for the specific landing site include (1) flat surface with low rock abundance, (2) thick regolith, and (3) small static magnetic field. Criterion 1 is for landing safety and low probability of interference with deployments (both on the surface and in the subsurface). Criterion 2 is to assure that the heat flow probe can penetrate up to several meters into the subsurface. Criterion 3 is to ensure that the measurements of time-varying magnetic fields can be performed in the highest sensitivity range and that the incoming fields are not locally distorted severely from plane-wave equivalents.

General Strategy. In selecting an exact location for landing the spacecraft in each of the aforementioned four areas proposed for the LGN mission (Figure 1), we consider science, engineering, logistical, and safety requirements for the individual payload instruments and the spacecraft. In identifying localities that satisfy these requirements, we use remote observations from either Earth or spacecraft orbiting around the Moon (Table 3). Here we use Mare Crisium as a case study for how each LGN detailed landing site analysis will be discussed.

Crustal Thickness. Mare Crisium is chosen as one of the four landing areas for the LGN mission, because it is an ideal location for constraining the thermal structure of the mantle away from the PKT. Heat flow through the surface of the basin should be least affected by the radiogenic heat production within the thin (∼10 km), mafic crust (Wieczorek et al. 2013; Arivazhagan & Karthi 2018). In narrowing down the potential area for landing, we start with the area inside the 10 km crustal thickness contour (Figure 8). This wide area of relatively flat topography and little variability in crustal thickness and composition should make geologic interpretation of the data acquired by the LGN mission relatively straightforward.

Magnetic Anomalies. To ensure that the measurements of time-varying magnetic fields by the MT instrument can be

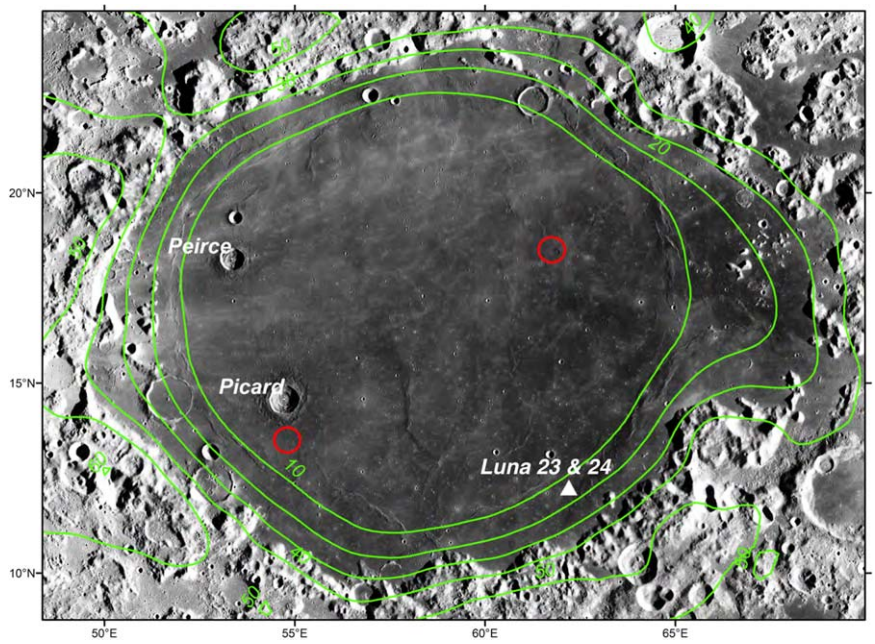

Figure 8. Contours (10 km intervals) of crustal thickness estimated from the GRAIL data (Wieczorek et al. 2013) drawn over a mosaic of images obtained by the LRO Wide Angle Camera (WAC) of Mare Crisium. The red circles indicate the two candidate areas for further consideration for landing site selection. The white triangle indicates the landing sites of Luna 23 and 24. The two spacecraft landed within 2–3 km of each other (Lawrence 2013). Only Luna 24 was able to return samples to Earth.

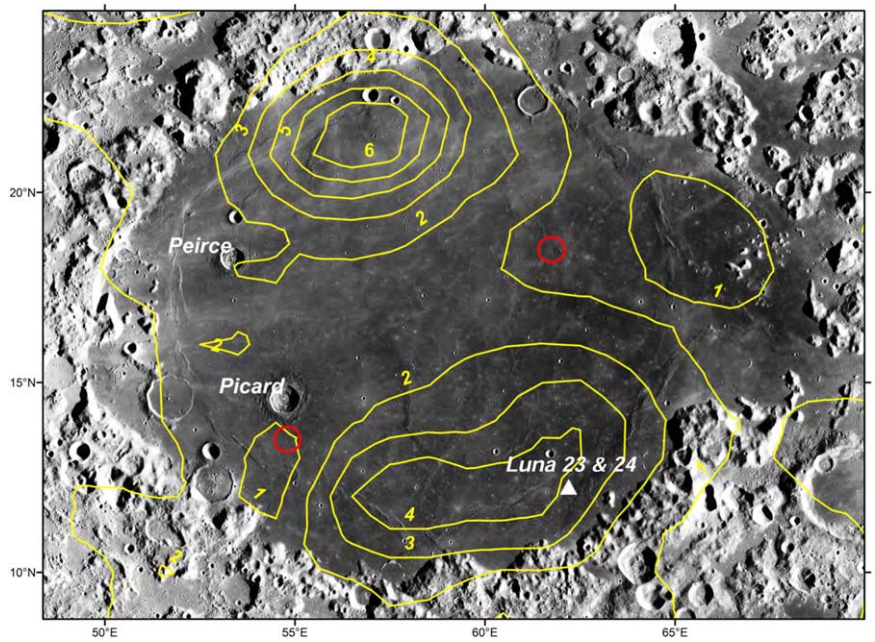

Figure 9. Contours (1 nT intervals) of magnetic anomaly intensity obtained at 30 km altitude by the Kaguya spacecraft (http://darts.isas.jaxa.jp/planet/pdap/selene/index.html.en), drawn over the LRO-WAC mosaic of Mare Crisium. The red circles indicate the two candidate areas for further consideration for landing site selection. The white triangle indicates the landing sites of Luna 23 and 24. See text for description of surface fields.

performed in the highest sensitivity range with minimum distortion of the incoming time-varying fields by any localized plasma, the lander should avoid obvious sites of high static magnetic field and plasma−surface interaction, namely, swirls. Because surface fields at these locations could be hundreds to thousands of nT, we seek sites <100 nT as a conservative bound. Mare Crisium has "bull's-eye" magnetic anomalies on both the north and south margins (Figure 9). The maximum total field at 30 km altitude ∼6 nT for the northern anomaly is modeled to be a maximum 60 nT at the surface (Baek et al. 2019; see also Tsunakawa et al. 2014). However, earlier modeling of the northern source (Hood 2011), as well as simple comparison of measured surface versus orbital magnetic fields (especially the Descartes swirl near A16; Dyal et al. 1973), suggests that surface fields in Mare Crisium could be as high as several hundred nT. Nonetheless, suitable sites <1 nT at 30 km, and therefore likely <10–100 nT at the surface, can be identified in Figure 9.

Regolith Properties. An optimal landing site must also have a relatively thick accumulation of regolith devoid of large rocks so that the heat flow probe can penetrate to 2–3 m depth. The

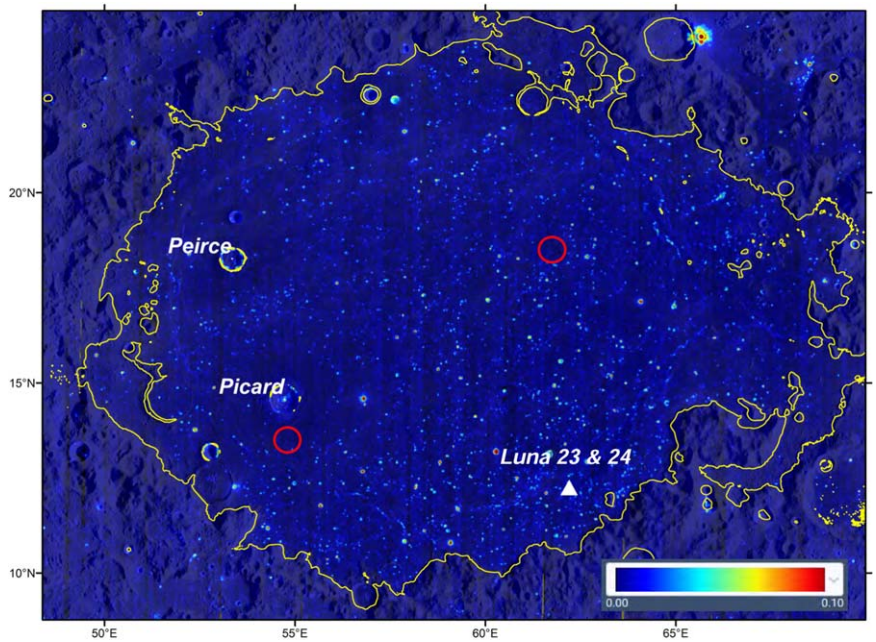

Figure 10. A map of rock abundance or concentration estimates derived from observations of the diurnal temperature swings by the LRO-diviner instrument (Bandfield et al. 2011). For each pixel, the fraction of the rock-covered area is given (0–0.1 color bar). Yellow lines are −3 km elevation contours that roughly define the extent of mare basalt fill within Crisium. The red circles indicate the two candidate areas for further consideration for landing site selection. The white triangle indicates the landing sites of Luna 23 and 24. Map data from Lunar QuickMap, available at https://bit.ly/32KYV5O.

presence of large rocks exposed on the surface can be inferred from the observation of the diurnal swing of thermal infrared waves, and that is how the rock abundance estimates (Figure 10) are obtained from the Diviner instrument on board NASA's LRO (Bandfield et al. 2011). To infer subsurface properties of the regolith, observation of the Earth-based, long-wavelength radar returns has been found effective. Radar waves can penetrate ∼10 times the wavelength into the subsurface. Fa & Wieczorek (2012) estimate the regolith in Mare Crisium to be 4–7 m thick throughout, based on the *P*-band (70 cm wavelength) radar returns received at the Arecibo Observatory.

Buried blocky objects scatter and reflect radar signals with wavelength up to 10 times their size. Regolith relatively devoid of large rocks in the 1−7 m depth range shows up as dark areas in circular polarization ratio (CPR) images of the *S*-band (12.6 cm wavelength) and *P*-band radar returns. It has been noted by previous observations (Ghent et al. 2010, 2016) that fine-grained ejecta deposited some distance away from medium-to-large-size craters show up as "dark halos" in *P*-band CPR images. In Mare Crisium, such halos are observed around Picard and Peirce (Figure 11). Surface rock abundance is also low in these radar-dark halos (Figure 10).

Based on these observations, we have chosen two areas of 10 km radius for further consideration for landing the spacecraft. The one is located in the radar-dark halo of Picard, which is sufficiently far away from the two bull's-eye magnetic anomalies. The other is located in a radar-dark area not associated with craters in the central basin where crustal magnetic anomalies are the lowest (Figures 8 and 10).

Surface Topography. Selecting a landing site within either of these two localities requires detailed knowledge of the topography. Safe landing of the spacecraft requires a wide, smooth, and level surface. Most of the payload instruments also require a wide, flat, and level surface for their optimal performances; the seismometer for good mechanical coupling with the ground, the retroreflector for an unobstructed line of sight to Earth, and the heat flow probe for penetrating vertically into the regolith.

In identifying areas of smooth, level surface, we first utilize the digital elevation model (DEM) that combines data from the Lunar Orbiter Laser Altimeter on board LRO and the laser altimeter on board Kaguya (Barker et al. 2016). This DEM has global coverage with 60 m spatial resolution and is well suited for identifying large-to-medium-size craters and other major positive- and negative-relief, basin-related, tectonic features such as wrinkle ridges and graben that may be hazardous to landers (Figure 12).

Even though much of the surface of the Mare Crisium appears smooth on these DEMs, higher spatial resolution imagery (1–2 m, LROC Narrow Angle Camera, NAC) reveals that the surface is peppered with a number of small-diameter (<10 m) craters. The LRO team is planning to acquire NAC stereo images over our two candidate areas in 2020–2021. For selecting an exact landing location, we will use the digital terrain model derived from the stereo images.

5. Conclusions

We have demonstrated the science driving network landing site selection for the LGN mission concept. These stations greatly improve on the previous measurements made during Apollo and will provide key observations advancing knowledge of the lunar interior. While some of our science objectives may be accomplished with a single station, the full network, in the baseline or threshold configurations, is needed to provide sufficient science return. Optimization of network sites will at least double the rate of detection of lower mantle and core phases over the Apollo network. The wide distribution of stations also improves the density of seismic

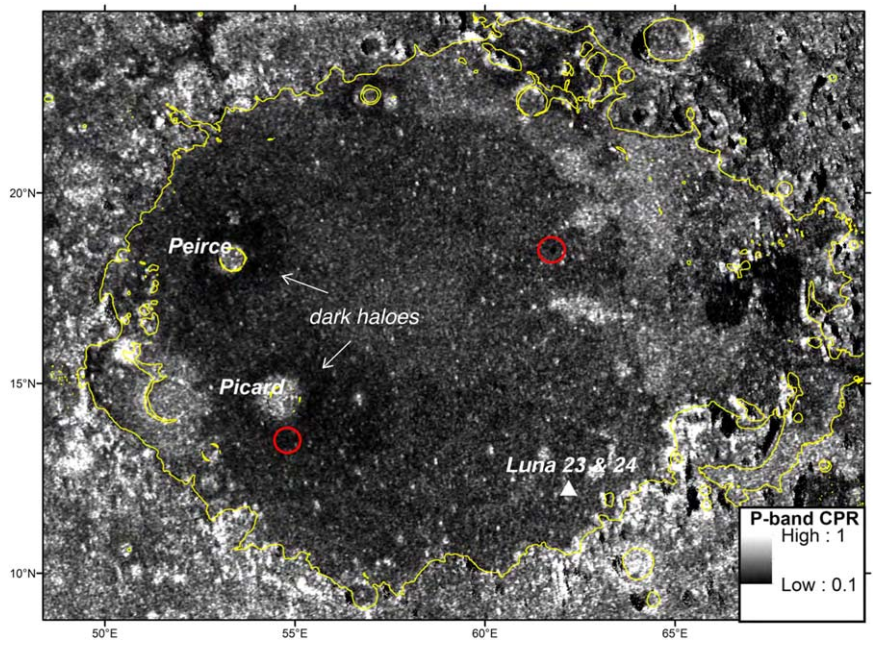

Figure 11. CPR image for the *P*-band radar returns obtained at the Arecibo Observatory (https://pds-geosciences.wustl.edu/missions/lunar_radar/index.htm). Yellow lines are −3 km elevation contours that roughly define the basin rims of Crisium. The white arrows point to the dark halos around craters Peirce and Picard. The red circles indicate the two candidate areas for further consideration for landing site selection. The white triangle indicates the landing sites of Luna 23 and 24.

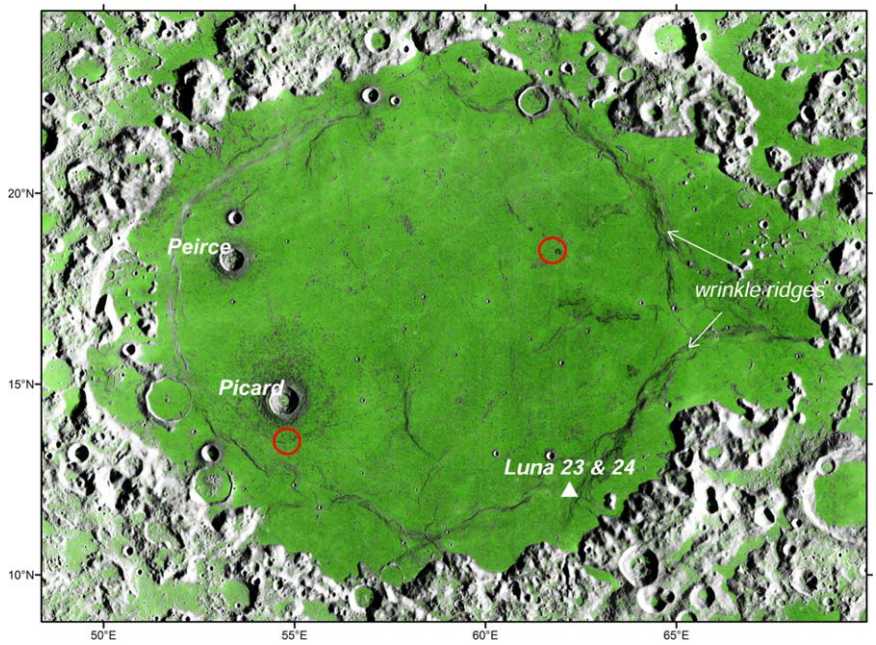

Figure 12. The areas of slope less than 4° are shown in green over the LRO-WAC mosaic, derived from the SLDEM (Barker et al. 2016) with 60 m spatial resolution. The white arrows point to some of the wrinkle ridges. The red circles indicate the two candidate areas for further consideration for landing site selection. The white triangle indicates the landing sites of Luna 23 and 24.

rays observed. NGLR improves the LLR network by pushing the stations toward the limbs with next-generation reflectors. This long-lived (>50 yr) ongoing program contributes to both geophysics and astrophysics, with projected improvements indicating ∼100× better accuracy. Heat flow and electromagnetics benefit from observations at multiple distinct locations representative of the lateral variability in internal structure. Once the network sites have been placed globally, locations within each landing site need to be analyzed across the spacecraft and instrument needs. We have demonstrated this methodology at the Crisium Basin as one example. Future work will apply this methodology to each of the proposed LGN landing sites. These example landing sites will continue to be evaluated and analyzed throughout the development of the LGN mission. This will include detailed analyses conducted at each network location, and updates will be evaluated across the primary and secondary mission requirements.

The authors acknowledge the National Aeronautics Space Administration grant number 80NSSC20K0154, Planetary Mission Concept Study, where the concept for this manuscript was initiated. D.C. acknowledges that his research was carried out at the Jet Propulsion Laboratory, California Institute of Technology, under a contract with the National Aeronautics and Space Administration (80NM0018D0004) and at the University of Maryland, College Park, under a contract with Notre Dame University (203769UMD). M.P. was supported by funds from the Jet Propulsion Laboratory, California Institute of Technology, and H.H., R.W., P. B. were supported by funds from the Marshall Space Flight Center, under contracts with the National Aeronautics and Space Administration. We acknowledge the use of imagery from Lunar QuickMap (https://quickmap.lroc.asu.edu), a collaboration between NASA, Arizona State University, and Applied Coherent Technology Corp. Any use of trade, firm, or product names is for descriptive purposes only and does not imply endorsement by the U.S. Government.

Appendix

This appendix includes three items: (1) links to LRO quickmap for the example landing sites discussed in the text; (2) Figure A1, which compares crustal thickness to Thorium concentration for each site; and (3) Table A1, which contains a list of acronyms used in the manuscript. LRO Quickmap links to LGN example landing sites:

1. PKT: https://bit.ly/31LdM0e
2. Schickard: https://bit.ly/3kyx5kF
3. Crisium: https://bit.ly/3jtlv91
4. Korolev: https://bit.ly/35DNjTc

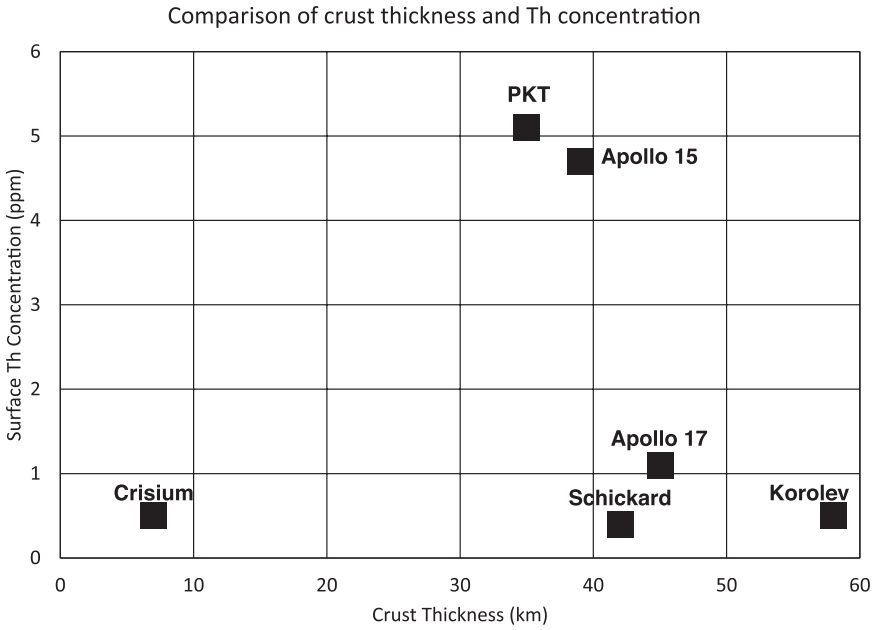

Figure A1. A scatter plot comparing the surface thorium concentration (ppm) and crust thickness of the A15 and 17 sites and the proposed landing sites for the LGN mission.

Table A1
Acronym List

ALSEP	Apollo Lunar Surface Experiment
APOLLO	Apache Point Observatory Lunar Laser-ranging Operation
CCRs	Cube Corner Retroreflectors
CLPS	Commercial Lunar Payload Services
CMB	Core–Mantle Boundary
CPR	Circular Polarization Ratio
DEM	Digital Elevation Model
DMQ	Deep Moonquakes
DTM	Digital Terrain Model
ELGO	European Lunar Geophysical Observatory
EM	Electromagnetic
FHT	Feldspathic Highlands Terrain
GR	General Relativity
GRAIL	Gravity Recovery and Interior Laboratory
KREEP	Potassium, Rare-Earth Elements, Phosphorus
LGN	Lunar Geophysical Network
LISTER	Lunar Instrumentation for Subsurface Thermal Exploration with Rapidity
LKFM	Low-K Fra Mauro
LLR	Lunar Laser Retroreflector
LLRO	Lunar Laser Ranging Observatories
LMAG	Lunar Magnetometer (Kaguya/SELENE)
LMS	Lunar Magnetotelluric Sounder
LOLA	Lunar Orbiter Laser Altimeter
LP	Lunar Prospector
LP	Long Period
LRO	Lunar Reconnaissance Orbiter
LROC	Lunar Reconnaissance Orbiter Camera
LSITP	Lunar Surface Instrument and Technology Payloads
MT	Magnetotelluric Method
NAC	Narrow Angle Camera
NGLR	Next Generation Lunar Retroreflectors
PcP	Core-Reflected P-wave
PKP	Core-Traversing P-wave
PKT	Procellarum KREEP Terrane
ScS	Core-Reflected Shear Wave
SEIS	Seismic Experiment for Interior Structure
SLR	Satellite Laser Ranging
SMQ	Shallow Moonquake
SP	Short Period
SSP	Silicon Seismic Package
SPA	South Pole–Aitken Basin
TF	Magnetic Transfer Function
VBB	Very Broad Band
VPREMOON	Very Preliminary REference MOON model
WAC	Wide Angle Camera

ORCID iDs

Heidi Fuqua Haviland https://orcid.org/0000-0001-5942-0585
Renee C. Weber https://orcid.org/0000-0002-1649-483X
Clive R. Neal https://orcid.org/0000-0003-0705-3490
Philippe Lognonné https://orcid.org/0000-0002-1014-920X
Raphaël F. Garcia https://orcid.org/0000-0003-1460-6663
Nicholas Schmerr https://orcid.org/0000-0002-3256-1262
Seiichi Nagihara https://orcid.org/0000-0002-4110-8398
Robert Grimm https://orcid.org/0000-0002-7588-1194
Simone Dell'Agnello https://orcid.org/0000-0002-0691-8213
Thomas R. Watters https://orcid.org/0000-0001-6756-6066
Mark P. Panning https://orcid.org/0000-0002-2041-3190
Catherine L. Johnson https://orcid.org/0000-0001-6084-0149
Martin Knapmeyer https://orcid.org/0000-0003-0319-2514
Lillian R. Ostrach https://orcid.org/0000-0002-3107-7321
Taichi Kawamura https://orcid.org/0000-0001-5246-5561
Noah Petro https://orcid.org/0000-0003-4676-077X
Paul M. Bremner https://orcid.org/0000-0002-3384-2613

References

Anderson, D. L. 1975, JGR, 80, 1555
Arivazhagan, S., & Karthi, A. 2018, P&SS, 161, 41
Baek, S., Kim, K., Garrick-Bethell, I., & Jin, H. 2019, JGRE, 124, 223
Bandfield, J. L., Ghent, R. R., Vasavada, A. R., et al. 2011, JGRE, 116, E00H02
Banks, M. E., Bensi, M., Schleicher, L. S., et al. 2020, AGUFM, 2020, P062-05
Banks, M. E., Watters, T. R., Robinson, M. S., et al. 2012, JGRE, 117, E00H11
Barker, M. K., Mazarico, E., Neumann, G. A., et al. 2016, Icar, 273, 346
Barr, J. A., & Grove, T. L. 2013, GeCoA, 106, 216
Bart, G. D., Nickerson, R. D., Lawder, M. T., & Melosh, H. J. 2011, Icar, 215, 485
Binder, A. B. 1982, M&P, 26, 117
Bonnell, J. W., Mozer, F. S., Delory, G. T., et al. 2008, in The THEMIS Mission, ed. J. L. Burch & V. Angelopoulos (New York: Springer), 303
Boyce, J. M., & Johnson, D. A. 1977, LPSC, 8, 3495
Brown, S. M., & Elkins-Tanton, L. T. 2009, E&PSL, 286, 446
Bulow, R. C., Johnson, C. L., & Shearer, P. M. 2005, JGRE, 110, E10003
Chabé, J., Courde, C., Torre, J., et al. 2020, E&SS, 7, e00785
Chapront, J., Chapront-Touzé, M., & Francou, G. 1999, in IAU Coll. 172, Impact of Modern Dynamics in Astronomy, ed. J. Henrard & S. Ferraz-Mello (Cambridge: Cambridge Univ. Press), 317
Charlier, B., Grove, T. L., & Zuber, M. T. 2013, E&PSL, 363, 50
Chave, A. D., & Jones, A. G. 2012, The Magnetotelluric Method: Theory and Practice (Cambridge: Cambridge Univ. Press)
Chenet, H., Lognonné, P., Wieczorek, M., & Mizutani, H. 2006, E&PSL, 243, 1
Cohen, B. A., Veverka, J., Banerdt, B., et al. 2009, ILN Final Report, Science Definition Team for the ILN Anchor Nodes, NASA, https://sservi.nasa.gov/wp-content/uploads/drupal/ILN_Final_Report.pdf
Costello, E. S., Ghent, R. R., Hirabayashi, M., & Lucey, P. G. 2020, JGRE, 125, e06172
Costello, E. S., Ghent, R. R., & Lucey, P. G. 2018, Icar, 314, 327
Crotwell, H. P., Owens, T. J., & Ritsema, J. 1999, Seismological Research Letters, 70, 154
Currie, D. G., Dell'Agnello, S., Delle Monache, G. O., Behr, B., & Williams, J. G. 2013, NuPhS, 243, 218
de Vries, D. A., & Peck, A. J. 1958, AuJPh, 11, 255
Drożdżewski, M., Sośnica, K., Zus, F., & Balidakis, K. 2019, JGeod, 93, 1853
Dyal, P., Parkin, C. W., & Cassen, P. 1972, LPSC, 3, 2287
Dyal, P., Parkin, C. W., & Daily, W. D. 1973, LPSC, 4, 2925
Eckhardt, D. H. 1993, in Interactions Between Physics and Dynamics of Solar System Bodies, ed. E. Bois, P. Oberti, & J. Henrard (Dordrecht: Springer), 307
Elkins-Tanton, L. T. 2008, E&PSL, 271, 181
Elkins-Tanton, L. T., Burgess, S., & Yin, Q.-Z. 2011, E&PSL, 304, 326
Elkins-Tanton, L. T., Chatterjee, N., & Grove, T. L. 2003, M&PS, 38, 515
Elkins-Tanton, L. T., Van Orman, J. A., Hager, B. H., & Grove, T. L. 2002, E&PSL, 196, 239
Erwin, A., Stone, K. J., Shelton, D., et al. 2020, LPSC, 51, 1034
Fa, W., Liu, T., Zhu, M. H., & Haruyama, J. 2014, JGRE, 119, 1914
Fa, W., & Wieczorek, M. A. 2012, Icar, 218, 771
Fayon, L., Knapmeyer-Endrun, B., Lognonné, P., et al. 2018, SSRv, 214, 119
Filiberto, J., Trang, D., Treiman, A. H., & Gilmore, M. S. 2020, SciA, 6, eaax7445
Fok, H. S., Shum, C. K., Yi, Y., et al. 2011, EP&S, 63, 15
Gagnepain-Beyneix, J., Lognonné, P., Chenet, H., Lombardi, D., & Spohn, T. 2006, PEPI, 159, 140
Garcia, R., Wieczorek, M., Kawamura, T., et al. 2020, Ideas For Exploring The Moon With A Large European Lander, European Lunar Geophysical Observatory, IDEA I-2020-02087, https://ideas.esa.int/servlet/hype/IMT?documentTableId=45087666723168969&userAction=Browse&searchTerm=SURFQSBJLTIwMjAtMDIwODc&templateName=&documentId=49ea79ae25c541011de44d84f66fdf43&searchContextId=cf0b62e8960e063eba8da635303a2581
Garcia, R. F., Gagnepain-Beyneix, J., Chevrot, S., & Lognonné, P. H. 2011, PEPI, 188, 96
Gault, D. E., Hörz, F., Brownlee, D. E., & Hartung, J. B. 1974, LPSC, 5, 2365

Ghent, R. R., Carter, L. M., Bandfield, J. L., Tai Udovicic, C. J., & Campbell, B. A. 2016, Icar, 273, 182
Ghent, R. R., Gupta, V., Campbell, B. A., et al. 2010, Icar, 209, 818
Giardini, D., Lognonné, P., Banerdt, W. B., et al. 2020, NatGe, 13, 205
Gillet, K., Margerin, L., Calvet, M., & Monnereau, M. 2017, PEPI, 262, 28
Grimm, R. E. 2013, JGRE, 118, 768
Grimm, R. E., & Delory, G. T. 2012, AdSpR, 50, 1687
Hartmann, W. K. 1999, M&PS, 34, 167
Hiesinger, H., Head, J. W., Wolf, U., Jauman, R., & Neukum, G. 2011a, GSA Special Papers, Vol. 477, Recent Advances and Current Research Issues in Lunar Stratigraphy (McLean, Va: GSA)
Hiesinger, H., Head, J. W., III, Wolf, U., Jaumann, R., & Neukum, G. 2003, JGRE, 108, 5065
Hiesinger, H., van der Bogert, C. H., Reiss, D., & Robinson, D. M. 2011b, EPSC-DPS Joint Meeting, 2011, 1095
Hirabayashi, M., Howl, B. A., Fassett, C. I., et al. 2018, JGRE, 123, 527
Hofmann, F., & Müller, J. 2018, CQGra, 35, 035015
Hood, L. L. 1986, in Origin of the Moon; Proc. Conf. (Houston, TX: Lunar and Planetary Inst.), 361
Hood, L. L. 2011, Icar, 211, 1109
Hood, L. L., Herbert, F., & Sonett, C. P. 1982, JGRE, 87, 5311
Hood, L. L., & Jones, J. H. 1987, JGRB, 92, E396
Hood, L. L., & Schubert, G. 1978, LPSC, 9, 3125
Hood, L. L., & Sonett, C. P. 1982, GeoRL, 9, 37
Hörz, F., Grieve, R., Heiken, G., Spudis, P., & Binder, A. 1991, in Lunar Sourcebook: A User's Guide to the Moon, ed. G. H. Heiken, D. T. Vaniman, & B. M. French (Cambridge: Cambridge Univ. Press), 61
Ikoma, M., Elkins-Tanton, L., Hamano, K., & Suckale, J. 2018, SSRv, 214, 76
Jolliff, B. L., Gillis, J. J., Haskin, L. A., Korotev, R. L., & Wieczorek, M. A. 2000, JGRE, 105, 4197
Kawamura, T., Lognonné, P., Nishikawa, Y., & Tanaka, S. 2017, JGRE, 122, 1487
Khan, A., Connolly, J. A. D., Olsen, N., & Mosegaard, K. 2006a, E&PSL, 248, 579
Khan, A., Connolly, J. A. D., Pommier, A., & Noir, J. 2014, JGRE, 119, 2197
Khan, A., Maclennan, J., Taylor, S. R., & Connolly, J. A. D. 2006b, JGRE, 111, E05005
Khan, A., & Mosegaard, K. 2002, JGRE, 107, 5036
Khan, A., Mosegaard, K., & Rasmussen, K. L. 2000, GeoRL, 27, 1591
Khan, A., Pommier, A., Neumann, G. A., & Mosegaard, K. 2013, Tectp, 609, 331
Korotev, R. L. 2000, JGRE, 105, 4317
Kumar, P. S., Mohanty, R., Lakshmi, K. J. P., et al. 2019, GeoRL, 46, 7972
Kumar, P. S., Sruthi, U., Krishna, N., et al. 2016, JGRE, 121, 147
Kuskov, O. L., Kronrod, E. V., & Kronrod, V. A. 2019, PEPI, 286, 1
Kuskov, O. L, Kronrod, V. A, & Hood, L. L 2002, PEPI, 134, 175
Kuskov, O. L., Kronrod, V. A., & Kronrod, E. V. 2014, PEPI, 235, 84
Lammlein, D. R., Latham, G. V., Dorman, J., Nakamura, Y., & Ewing, M. 1974, RvGeo, 12, 1
Laneuville, M., Taylor, J., & Wieczorek, M. A. 2018, JGRE, 123, 3144
Langseth, M. G., Keihm, S. J., & Peters, K. 1976, LPSC, 7, 3143
Lawrence, D. J., Feldman, W. C., Barraclough, B. L., et al. 2000, JGRE, 105, 20307
Lawrence, S. 2013, LROC Coordinates of Robotic Spacecraft—2013 Update, http://lroc.sese.asu.edu/posts/650
Le Feuvre, M., & Wieczorek, M. A. 2011, Icar, 214, 1
Lognonné, P., Banerdt, W. B., Giardini, D., et al. 2019, SSRv, 215, 12
Lognonné, P., Banerdt, W. B., Pike, W. T., et al. 2020, NatGe, 13, 213
Lognonné, P., Gagnepain-Beyneix, J., & Chenet, H. 2003, E&PSL, 211, 27
Lognonné, P., & Johnson, C. L. 2015, Treatise on Geophysics (Amsterdam: Elsevier), 65
Lognonné, P., Le Feuvre, M., Johnson, C. L., & Weber, R. C. 2009, JGRE, 114, E12003
Longhi, J. 1992, GeCoA, 56, 2235
Longhi, J. 1993, LPSC, 24, 895
Longhi, J., Walker, D., Grove, T. L., Stolper, E. M., & Hays, J. F. 1974, LPSC, 5, 447
Lunar Exploration Analysis Group 2017, Advancing Science of the Moon: Report of the Specific Action Team, https://www.lpi.usra.edu/leag/reports/ASM-SAT-Report-final.pdf
Masoumi, S., McClusky, S., Koulali, A., & Tregoning, P. 2017, JGRD, 122, 4401
Maurice, M., Tosi, N., Samuel, H., et al. 2017, JGRE, 122, 577
McCulloch, M. T. 1987, in Proterozic Lithospheric Evolution, ed. A. Kröner, Vol. 17 (New York: Wiley), 115
Mighani, S., Wang, H., Shuster, D. L., et al. 2020, SciA, 6, eaax0883
Moser, D. E., Suggs, R. M., Kupferschmidt, L., & Feldman, J. 2015, Lunar Impact Flash Locations from NASA's Lunar Impact Monitoring Program, NASA Technical Memorandum 20150021386, https://ntrs.nasa.gov/citations/20150021386
Murphy, T. W., Strasburg, J. D., Stubbs, C. W., et al. 2004, in Proc. 14th Int. Workshop on Laser Ranging, APOLLO: Meeting the Millimeter Goal (San Fernando), 165
Nagihara, S., & Grimm, R. 2020, A Proposal for Heat Flow Measurement and Magnetotelluric Sounding in Mare Imbrium, Abstract #5007
Nagihara, S., Ngo, P., Sanigepalli, V., et al. 2020, LPSC, 51, 1432
Nakamura, Y. 1983, JGRB, 88, 677
Nakamura, Y. 2005, JGRE, 110, E01001
Nakamura, Y., Dorman, J., Duennebier, F., et al. 1974, LPSC, 5, 2883
Nakamura, Y., Latham, G. V., Dorman, H. J., et al. 1979, LPSC, 10, 2299
Nakamura, Y., Latham, G. V., & Dorman, H. J. 1982, JGRB, 87, A117
National Research Council 2007, The Scientific Context for Exploration of the Moon (Washington, DC: The National Academies Press), https://doi.org/10.17226/11954
National Research Council 2011, Vision and Voyages for Planetary Science in the Decade 2013–2022 (Washington, DC: The National Academies Press), https://doi.org/10.17226/13117
Neal, C. R. 2001, JGRE, 106, 27865
Neal, C. R., Weber, R., Seas, A., et al. 2020, The Lunar Geophysical Network, Final Report. Planetary Mission Concept Study, https://science.nasa.gov/science-red/s3fs-public/atoms/files/Lunar%20Geophysical%20Network.pdf
Newhall, X. X., & Williams, J. G. 1997, in IAU Coll. 165, Estimation of the Lunar Physical Librations (Cambridge: Cambridge Univ. Press), 21
Nimmo, F., Faul, U. H., & Garnero, E. J. 2012, JGRE, 117, E09005
Nunn, C., Garcia, R. F., Nakamura, Y., et al. 2020, SSRv, 216, 89
Nunn, C., Pike, W. T., Panning, M. P., & Kedar, S. 2019, LPSC, 50, 2223
Nyquist, L. E., Wiesmann, H., Bansal, B. M., Wooden, J., & McKay, G. 1978, in Chemical and Sr-isotopic Characteristics of the Luna 24 Samples. Mare Crisium: The View from Luna 24, ed. R. B. Merill & J. J. Papike (New York: Pergamon Press), 631
Oberbeck, V. R., & Quaide, W. L. 1968, Icar, 9, 446
Oberst, J., & Nakamura, Y. 1992, in 2nd Conf. Lunar Bases and Space Activities, A Seismic Risk for the Lunar Base, Houston, TX, ed. W. W. Mendell, 231
Ortiz, J. L., Aceituno, F. J., Quesada, J. A., et al. 2006, Icar, 184, 319
Panning, M. P., Pike, W. T., Lognonné, P., et al. 2020, JGRE, 125, e06353
Qin, C., Muirhead, A. C., & Zhong, S. 2012, Icar, 220, 100
Quaide, W., & Oberbeck, V. 1975, Moon, 13, 27
Quaide, W. L., & Oberbeck, V. R. 1968, JGR, 73, 5247
Rambaux, N., & Williams, J. G. 2011, CeMDA, 109, 85
Richmond, N. C., & Hood, L. L. 2008, JGRE, 113, E02010
Shearer, C. K., Hess, P. C., Wieczorek, M. A., et al. 2006, RvMG, 60, 365
Shimizu, H., Matsushima, M., Takahashi, F., Shibuya, H., & Tsunakawa, H. 2013, Icar, 222, 3243
Silverberg, E. C., & Currie, D. G. 1971, JOSA, 61, 692
Simpson, F., & Bahr, K. 2005, Practical Magnetotellurics (Cambridge: Cambridge Univ. Press)
Smith, D. E., Zuber, M. T., Neumann, G. A., et al. 2017, Icar, 283, 70
Smith, J. V., Anderson, A. T., Newton, R. C., et al. 1970, GeCAS, 1, 897
Snyder, G. A., Neal, C. R., Taylor, L. A., & Halliday, A. N. 1997, GeCoA, 61, 2731
Snyder, G. A., Taylor, L. A., & Neal, C. R. 1992, GeCoA, 56, 3809
Sollberger, D., Schmelzbach, C., Robertsson, J. O. A., et al. 2016, GeoRL, 43, 10,078
Sonett, C. P. 1982, RvGeo, 20, 411
Sonett, C. P., Smith, B. F., & Colburn, D. S. 1972, LPSC, 3, 2309
Spohn, T., Grott, M., Smrekar, S. E., et al. 2018, SSRv, 214, 96
Stofan, E. R., Smrekar, S. E., Mueller, N., & Helbert, J. 2016, Icar, 271, 375
Taylor, S. R. 1982, Planetary Science: A Lunar Perspective (Houston, TX: LPI)
Taylor, S. R., & Jakes, P. 1974, LPSC, 5, 1287
Tsunakawa, H., Takahashi, F., Shimizu, H., Shibuya, H., & Matsushima, M. 2014, Icar, 228, 35
van der Bogert, C. H., Clark, J. D., Hiesinger, H., et al. 2018, Icar, 306, 225
Varghese, T. K., Decker, W. M., Crooks, H. A., & Bianco, G. 1993, Matera Laser Ranging Observatory (MLRO): An Overview, Report No. N94-15601, NASA, https://ntrs.nasa.gov/api/citations/19940011128/downloads/19940011128.pdf
Verhoeven, O., & Vacher, P. 2016, P&SS, 134, 29
Vinnick, L., Chenet, H., Gagnepain-Beyneix, J., & Lognonné, P. 2001, GeoRL, 28, 3031
Wagner, R. V., Nelson, D. M., Plescia, J. B., et al. 2017, Icar, 283, 92
Walker, D., Longhi, L., Stolper, E. M., Grove, T. L., & Hays, J. F. 1975, GeCoA, 39, 1219

Watters, T. R., & Johnson, C. L. 2010, in Planetary Tectonics, ed. T. R. Watters & R. A. Schultz (Cambridge: Cambridge Univ. Press), 121
Watters, T. R., Robinson, M. S., Banks, M. E., Tran, T., & Denevi, B. W. 2012, NatGe, 5, 181
Watters, T. R., Robinson, M. S., Beyer, R. A., et al. 2010, Sci, 329, 936
Watters, T. R., Robinson, M. S., Collins, G. C., et al. 2015, Geo, 43, 851
Watters, T. R., Weber, R. C., Collins, G. C., et al. 2019, NatGe, 12, 411
Weber, R. C., Bills, B. G., & Johnson, C. L. 2009, JGRE, 114, E05001
Weber, R. C., Bills, B. G., & Johnson, C. L. 2010, PEPI, 182, 152
Weber, R. C., Lin, P.-Y., Garnero, E. J., Williams, Q., & Lognonné, P. 2011, Sci, 331, 309
Weiss, B. P., & Tikoo, S. M. 2014, Sci, 346, 1198
Wieczorek, M. A., Neumann, G. A., Nimmo, F., et al. 2013, Sci, 339, 671
Wieczorek, M. A., & Phillips, R. J. 2000, JGRE, 105, 20417
Williams, J. G., & Boggs, D. H. 2015, JGRE, 120, 689
Williams, J. G., Boggs, D. H., Currie, D. G, et al. 2020, Lunar Laser Ranging on Artemis III: Operation and Scientific Goals. Artemis III Science Definition Team White Paper, 2073,https://www.lpi.usra.edu/announcements/artemis/whitepapers/2073.pdf
Williams, J. G., Boggs, D. H., & Ratcliff, J. T. 2013, LPSC, 44, 2377
Williams, J. G., Boggs, D. H., Yoder, C. F., Ratcliff, J. T., & Dickey, J. O. 2001, JGRE, 106, 27933
Williams, J. G., Konopliv, A. S., Boggs, D. H., et al. 2014, JGRE, 119, 1546
Williams, J. G., Newhall, X. X., & Dickey, J. O. 1996, P&SS, 44, 1077
Williams, J. G., Turyshev, S. G., & Boggs, D. H. 2004, PhRvL, 93, 261101
Williams, J. G., Turyshev, S. G., & Boggs, D. H. 2009, IJMPD, 18, 1129
Williams, J. G., Turyshev, S. G., & Boggs, D. H. 2012, CQGra, 29, 184004
Wood, J. A., Dickey, J., John, S., Marvin, U. B., & Powell, B. N. 1970, GeCAS, 1, 965
Yamada, R., Garcia, R. F., Lognonné, P., et al. 2011, P&SS, 59, 343
Yamada, R., Garcia, R. F., Lognonné, P., et al. 2013, P&SS, 81, 18
Yue, Z., Di, K., Liu, Z., et al. 2019, Icar, 329, 46